POLITECNICO DI TORINO

Master's Degree in Mechanical Engineering

Politecnico
di Torino

Master's Degree Thesis

Mechanical characterisation of lattice structures manufactured by Selective Laser Melting process (SLM)

Supervisors

Prof. Luca Iuliano

Prof. Abdollah Saboori

Candidate

Ubaldo Iannuzzo

A.a. 2020/2021

Acknowledgements

First of all, I would like to thank my supervisors, Prof. Luca Iuliano and Prof. Abdollah Saboori, who gave me the opportunity to do this thesis work. A special thanks also to Erika Lannunziata for the help and availability shown to me.

I would also like to say a few words about my family who have been with me throughout this long journey since the first day I arrived in Turin. To my parents who have supported my studies and who gave me everything whenever I needed it and who believed in me even when I didn't. It is mainly thanks to them that things have often gone in the right direction. Thanks also to Alberto, who has always encouraged me to do more, to do better. It is also thanks to you that I am this person today.

I would like to dedicate a special thanks to Team H2politO. They have welcomed me and taught me so much. In four years they have shown me what it means to be a winning team, how to face challenges, and, above all, they have given me many opportunities. They have made me grow a lot.

I would like to thank the whole family of Collegio Einaudi, my family on the third floor. I had the honor of meeting wonderful people, friends. The years I spent there are for sure a beautiful memory.

Finally, I would like to thank all the people I have met along this path. To those who have been with me during these years and those who have believed in me. Too many to mention you all.

And thanks to me too, for all the mistakes I have made. They have taught me more than any other victory.

Abstract

In the engineering sector, for several years now, the focus has been on optimisation of components, on the search for the perfect geometry that guarantees high mechanical properties but at the same time minimises mass. Searching for lightweight and also adequate mechanical properties has become increasingly common. Here, additive manufacturing plays a key role. Additive Manufacturing (AM) offers incredible design freedom for topologically complex components, that before the advent of this technology were manufactured with many difficulties and expenses. At the same time, it offers a wide range of materials.

Cellular structures, also called Lattices, are not a recent discovery. They are strongly present in nature (e.g. wood, cork, bones, etc.) and are still very common for large civil and construction works (e.g. the Eiffel tower). With the advent of additive manufacturing, it has been possible to start making these geometries, which most often have very complex shapes with very small dimensions. This makes them useful for many applications. and this is why a lot of emphases has been placed on this type of solution in the last 10 to 15 years. Some of the most important applications today are in the biomedical, automotive and aerospace industries. Thanks to their energy-absorbing capacity and lightweight.

The aim of this thesis is to study and characterise some structures produced by the SLM (Selective laser melting) process. Two different types of structures are considered, the strut-based structures based on strut elements and the TPMS (Triply Periodic Minimal Surfaces) generated from trigonometric functions. Specimens with different relative densities were made for the selected structures. The material analysed is SS 316L, which is widely used in various fields. The focus of this work was to investigate the stiffness behaviour as the characterising parameters vary. For this reason, static compression tests were performed, this allows the determination of values such as Young's modulus, UCS and also the amount

of energy absorbed. Finally, a numerical simulation was carried out to analyse the behaviour of the structures and highlight possible main directions of load application. The procedures and the techniques used in the experimental stage were explained both practically and theoretically.

Table of Contents

List of Tables

List of Figures

Acronyms

AM

Additive Manufacturing

CAD

Computer Aided Design

FEM

Finite Element Method

RD

Relative density

SLM

Selective laser melting

TPMS

Triply periodic minimal surface

UCS

Ultimate Compressive Strength

1 Introduction

This work is divided into 5 chapters. The first chapter, "Introduction", provides a quick overview of additive technology and its advantages. It also introduces the concept of lattice structures with definitions and a first classification. The second chapter, "State of Art", illustrates some theoretical concepts that are present today in the literature on the subject of cellular material. The strut-based cellular structures and TPMS ones are presented, behaviours are analysed and some of the most common geometries are illustrated. Some properties were then explained. The third chapter "Materials and Methods" opens the experimental part of this work. It describes the fabrication of the chosen structures and explains the various processes that led to the characterisation and detection of certain mechanical properties. In the fourth chapter, "Results and Discussions", the results obtained in the experiments are presented, with a focus on parameters such as Young's modulus, yield strength, and specific energy absorbed (SEA). A comparison with the Ashby-Gibson model is made and a numerical simulation is computed. Chapter 5 summarises the results obtained and concludes the work.

1.1 Additive Manufacturing

Additive Manufacturing (AM) is defined by the joint ISO/ASTM terminology standard as the "process of joining materials to make objects from 3D model data, usually layer upon layer, as opposed to subtractive manufacturing methodologies" [1]. It represents a clear reversal of trend compared to traditional production technologies practically based on the removal of material starting from full standard

geometries. One of the most important potentialities of AM consists in the fabrication of parts with great geometrical complexity. This aspect does not appear to exhibit limitations from a design point of view, providing accurate control (potentially down to the micrometre) of internal and external geometries [2] but it has also led to a radical change in how parts are conceived, designed and embedded in final products [3]. The strengths of this technology are represented by:

- The possibility of building relatively small size components and allowing for the fabrication of topologies that could not have been achieved using traditional fabrication techniques.
- The technology exhibits superb material consumption with very low scrap rates with the associated environmental and cost-benefit.
- The chance to minimize the mass of the component, due to the possibility of adding material only where it is needed to guarantee the desired properties.
- The ability to optimize assemblies by reducing the number of components.
- The possibility to easily create internal channels in the component.

Additive Manufacturing has become increasingly important in the past few decades due to the growing demand for the manufacture of components with complex geometries as well as high mechanical quality [4]. The appeal derives from its ease of implementation; where for the most part, a 3D computer model is all that is required to obtain a net or a near-net component. Over the past few years, studies and technology related to AM have grown rapidly with an annual growth rate of approximately 30% between 2010 and 2015 and estimated material sales projected to increase to $8 billion by 2025 [5]. AM has been deemed applicable to almost all industrial sectors, e.g. mechanical, automotive, aerospace and medical. The industry has a strong interest in structural lightweight concepts with high performances but at the same time with lower costs. For this reason, the attention in recent years has been shifting towards manufacturing techniques for cellular materials with a high strength to weight ratio, but also high impact resistance and energy absorption.

1.2 Cellular solids

Material with cellular structure is very common in nature, just think of materials like wood, cork, sponge and bone. They have been used by people for over 5000 years (e.g. in the Pyramids of Egypt) [6]. More recently man started to make his cellular materials in the form of honeycomb or foams. The properties of honeycomb ad foams, or cellular structure in general, are many. The small cell size and low volume fraction make them perfect for thermal insulators, thanks to their low compressive strength and high deformation capacity make them excellent as energy absorbers. Their low density makes them perfect as core material for lightweight structural sandwich panels [6]. In Figure 1.1 it's possible to see the ranges within which these materials operate. The variation of the design properties range is illustrated by Ashby and Gibson [7]. The influx of AM technologies enables the creation of lightweight objects due to either the use of porous structures [8], topological optimization or integrating three-dimensional lattice. AM brings an economical advantage to its consumer as regardless of the complexity of the components, manufacturing costs remain equal. (so that the production of geometrically complex structures can be more economical using AM). Fabricating complex cell geometries is extremely challenging, especially when the desired size scale gets smaller. The recent advances in additive manufacturing helped mitigate these challenges. For this reason, many new geometries have been created over the past few years.

1.3 Definition and classification

The terminology "lattice structures" appears in varied disciplines such as AM, structural and civil engineering, biological and material sciences and crystallography. For this reason, there is not a unique definition of what a lattice structure is. Ashby [9] defined a lattice as a connected network of struts with the purpose to create stiff, strong load-bearing structures using as little material as possible. Tao et al. defined lattice structure as an architecture formed by an array of spatial periodic unit cells with edges and faces (as cited by Pan). Pan et al. [10] defined lattice structures as three-dimensional structures composed of consecutively and repeatedly arranged

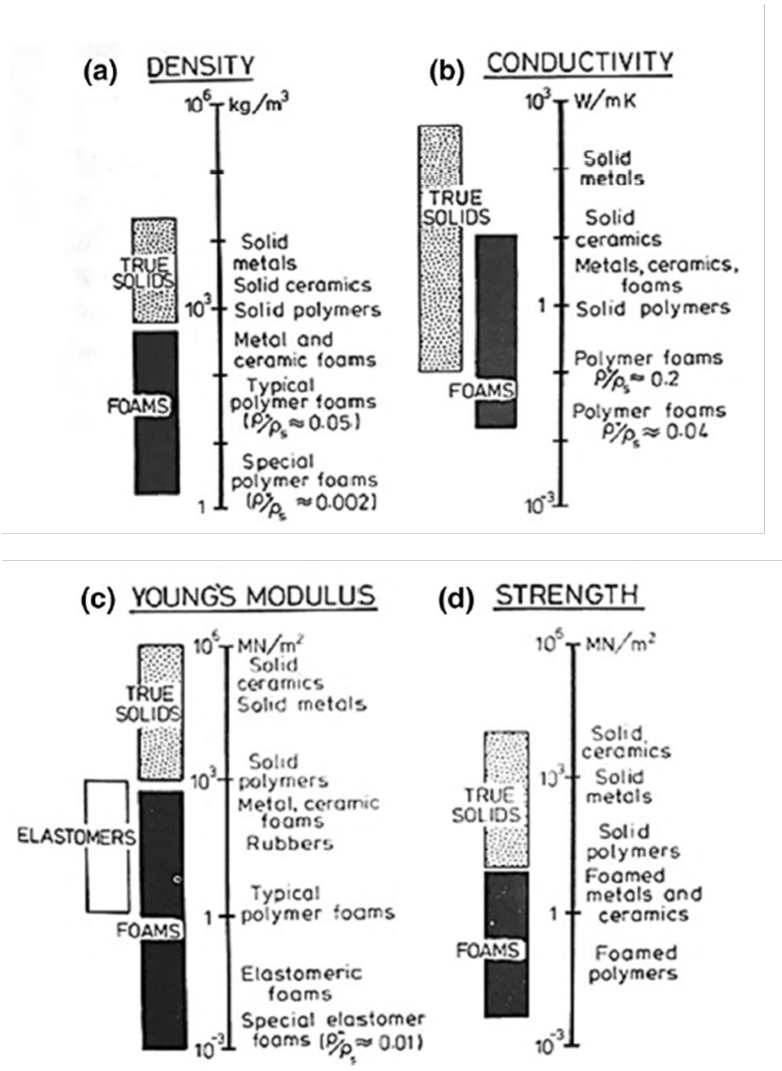

Figure 1.1: The range of properties available to the engineer through foaming: (a) density; (b) thermal conductivity; (c) Young modulus; (d) compressive strength [7]

interconnected cells, which can also be understood as a porous material structure composed of interconnected struts and nodes in a three-dimensional space. These definitions share the notion that lattice structure is a three-dimensional space structure. But as stated by Ashby, lattice materials differ from the lattice of the engineer in one important aspect: the scale. The unit cell of lattice materials is so small (down to micrometres) to allow them to be viewed both as structures and

as materials [9]. For this reason, it is possible to think of a lattice also linked to the properties of the material allowing comparison with the full, bulk material. According to the literature, there are different methods to classify lattice structures. Dong et al. [11] categorized them based on the degree of order of the lattice frame. Generally, there are three categories (shown in Figure 1.2):

1. Disordered lattice structures, also known as randomized lattice structures
2. Periodic lattice structures
3. Pseudo periodic lattice structures

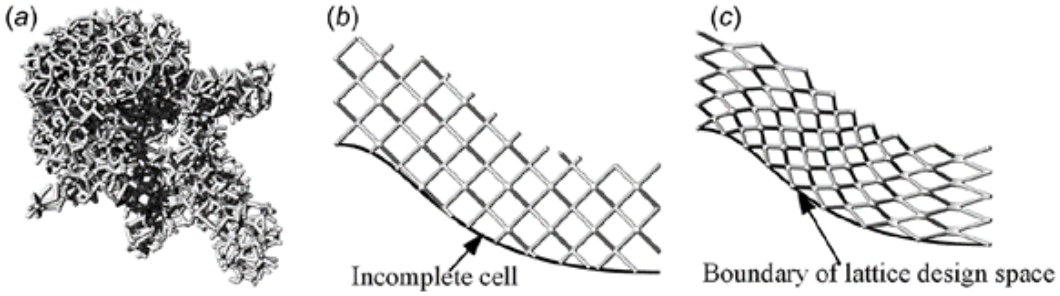

Figure 1.2: Examples of different types of lattice structures based on the degree of order: (a) disordered lattice structures, (b) periodic lattice structures, and (c) conformal lattice structures. [11]

Disordered lattice structures are characterised by randomly distributed unit cells, with different topologies and cell sizes. Periodic lattice structures are characterised by regular periodic repetition of a unit cell, featuring the same shape and topology in a three-dimensional Euclidean space. Pseudoperiodic lattice structures are characterised by cells that only share the same topology but different sizes and shapes. Another distinction can be made between open-cell, in which struts form the edges of the cell, and closed-cell, in which a solid membrane covers the cell faces.

2 State of art

To better understand the behaviours of lattice structures or more generally of cellular solids we have to identify which parameters are involved in the study and how they affect the final behaviour of the cell. Ashby [9] identified three variables to use as a starting point in the analysis:

1. The material of which it is made
2. The relative density
3. Cell topology and shape

The material influences mechanical, thermal and electrical solid properties. This work will focus solely on 316L stainless steel, invalidating the material's influence. Relative density (RD) is defined as the ratio between the density of the cellular material (ρ) and the density of the bulk material (ρ_s)

$$RD = \frac{\rho}{\rho_s} \tag{2.1}$$

To be defined as a cellular solid, relative density has to be lower than 0.3 [7]. Cell topology and shape are relevant to understanding the behaviour distinction between bending and stretching-dominated structures [9]. To fully understand the significant features of both bending and stretch dominated structures we have to use dimensional methods to obtain more simple and approximate scaling laws. An open-cell cellular solid can be treated as a connected set of pin-jointed frames as shown in Figure 2.1 . We can distinguish between a mechanism (a) and a structure (b). In a mechanism, the frame has one or more degrees of freedom and if we

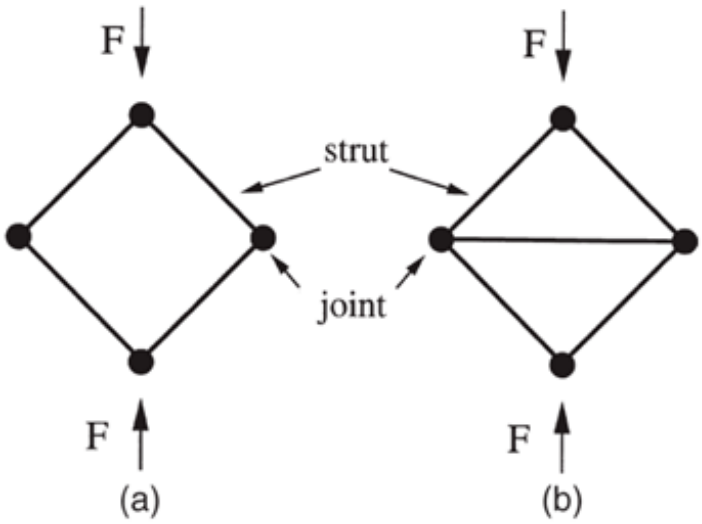

Figure 2.1: (a) A mechanism; (b) a structure. [12]

apply a load in one direction the struts rotate around the joints and the frame collapses. In contrast, the structure is statically stable, and external loads are equilibrated [12]. To easily understand the frames' behaviour, it is possible to introduce Maxwell's stability criterion. Maxwell [13] suggested an algebraic rule for a pin-jointed frame to be both statically and kinematically determinate. In Equation 2.2 and Equation 2.3 are reported the equations of Maxwell's criterion for a 2D and a 3D frame respectively, of b struts and j joints [14]:

$$M = b - 2j + 3 \tag{2.2}$$

$$M = b - 3j + 6 \tag{2.3}$$

According to Equations 2.2 and 2.3, if M is lower than 0, the lattice has too few struts to be statically determinant. The structure shows bending-dominated behaviour meaning that if an external load is applied fewer struts are present to equilibrate moments induced at the nodes, causing bending stresses. This lattice has high compliance and relatively low strength[9] [15]. If M = 0, the structure has the minimum number of struts required for it to be statically determinant. In this case, the structure exhibits stretch-dominated behaviour, relatively high stiffness

and strength [16]. Whereas if M > 0, the structure has an excess of struts required to achieve static equilibrium. In this case, the lattice exhibits a stretch dominated behaviour, external loads are equilibrated by axial tension and compression in struts, meaning that no bending occurs [17]. It is therefore possible to obtain a structure with high stiffness and strength thanks to the supporting effect of the extra strut elements. Slender structures are much stiffer when stretched than when bent. This principle defines stretch dominated structures with high structural efficiency [9]. Thanks to the Maxwell criteria it is possible to identify at first glance the structural efficiency of the cell. However, we must consider that this is not a sufficient condition for determining lattice structures rigidity. Rather, it is a useful tool to predict the performance of differing structure topologies. For example, from Figure 2.2, it is possible to see different periodic lattice structures with their relative Maxwell number [16].

Cell type	BCC	FCCZ	FBCCZ	FBCCXYZ	BCCZ	FCC
						
Struts, *s*	8	20	28	44	12	16
Joints, *n*	9	12	13	15	9	12
Maxwell number, *M*	−13	−10	−5	5	−9	−14
Strut aligned to load direction	No	Yes	Yes	Yes	Yes	No

Figure 2.2: Maxwell number for unit cell candidate lattice structures [Book: Laser Additive Manufacturing- Materials, Design, Technologies and Applications; Milan Brandt]

2.1 Response of cellular structure to loading

The behaviour of the structure is deeply present also in uniaxial compressive and tensile stress-strain curves. If the analysis is extended to all deformation fields

until the collapse of the cell is reached, it's possible to obtain the characteristic curve shown in Figure 2.3. The general deformation curve exhibit three main stages: the linear elastic deformation region (I), the plastic deformation (II) and the compaction area or densification (III). The main mismatched between different types of behaviour are present in the second area, in the plastic deformation field, whereas the first and the last part of the curve remain approximately the same. At low strain, the deformation mechanism is represented by a linear elastic behaviour, with elastic modulus E up to the elastic limit. Exceeded the yield strength value the plastic deformation begins. It's possible to distinguish two types of the characteristic curve, one for bending-dominated structure Figure 2.3 (a) and one for stretch-dominated ones Figure 2.3 (b).

Considering the bending dominated structure, it shows large plateau stress, a big area in which the stress keep constant increasing the strain. This region of the graph is important because in some way represent the amount of energy stored by the cell (proportional to the area under the graph) until the failure. For this reason, considering the high deformation capability, having large plateau stress is an important condition for all energy absorption applications. Considering the stretch dominated case, the curve exhibits a higher value of yield strength but can show post-yield softening. In this case, as was stated before, the mechanisms of deformation involve practically only tension and compression modes ('hard' modes) rather than bending ones ('soft'), this implies that initial yield is followed by plastic buckling or brittle collapse of the struts, leading to post-yield softening. For this reason, this kind of structure is less good for energy absorbing applications that require, ideally, a stress-strain curve with a long, flat plateau. Due to these properties, such structure can be used for lightweight design, as load-bearing components or sandwich cores [Fiber-Reinforced Composite Sandwich Structures by Co-Curing with Additive Manufactured Epoxy Lattices] Finally, it comes to densification of the collapsed lattice structure (III). It is characterized by a significant increase in stress. Densification in a purely geometric effect, due to the fact that formerly opposing unit cell walls come into contact and further bending is not possible.

The modulus and initial yield strength of stretching dominated structures are much greater than those of bending dominated structures of the same relative

density due to their different collapse modes and hence, are more weight-efficient for structural applications. The tensile behaviour is slightly different. The linear elastic part is always present, but the stress plateau disappears for some kind of material, instead of crashing progressively [6][18].

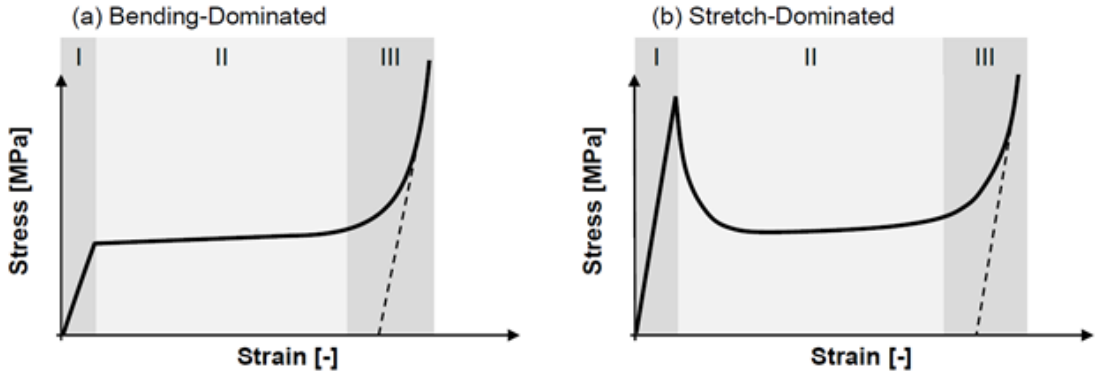

Figure 2.3: Compression behavior of bending-dominated (a) and stretch- dominated (b) lattice structures

Another large series is made up of lattice structure with graded porosity (illustrated in section 2.5). This kind of lattice structure is widely used in the medical field because it very faithfully replicates the internal composition of the bones. The stress-strain curves of graded lattice specimens are shown in Figure 2.4. The black line indicates the predicted form of the stress-strain curve calculated upon the data obtained from the tests conducted on uniform lattice structures, while the coloured lines indicate the stress-strain curves obtained for all three graded specimens. All curves showed a clear collapse on the individual layer.

A formulation for predicting the Young modulus of a graded lattice structure has been proposed assuming a simple series of uniform layers of the same thickness. In the iso-stress conditions that correspond to axial compression, the rule of the mixture has been applied to calculate the elastic modulus of the whole structure:

$$\frac{1}{E_{graded}} = \frac{1}{3E_1} + \frac{1}{3E_2} + \frac{1}{3E_3} \tag{2.4}$$

In Equation 2.4 E_{graded} is the Young modulus of the graded lattice structure, whereas E_1, E_2, and E_3 are the Young modulus of each layer of the whole structure.

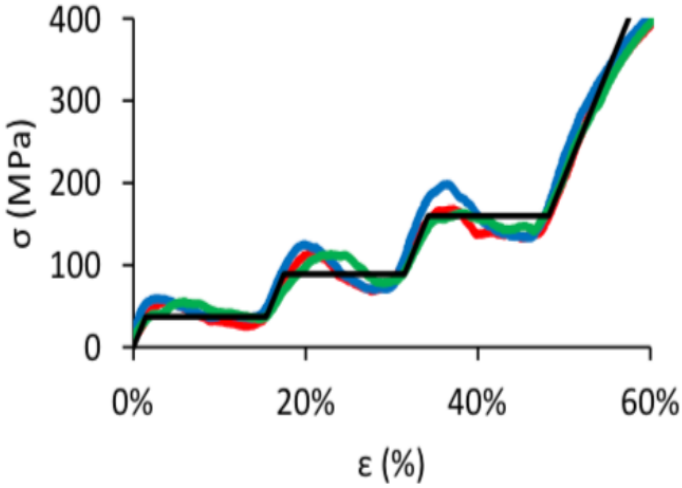

Figure 2.4: Compression behavior graded lattice structures

This result is useful in the design process of orthopedic implants in which the possibility to tune the mechanical characteristics and the relative density according to the properties of the actual bone structure could be a turning point for this kind of application in the medical sector.

Lei et al. [19] have evaluated the mechanical performance end so the stress-strain curve behaviour by changing the number of layers of the tested specimens, with constant relative density and constant geometries. In general, the mechanical performance has shown an inverse relationship with the number of layers. Increasing the number of layers resulted in a decrease in the stiffness and ultimate strength as is possible to notice in Figure 2.5. This behaviour can also be seen in the fracture of the specimens as shown in Figure 2.6. For the three-layer structures, layer-by-layer damage was shown: this led to a stress-strain curve with several peaks. In contrast, for the five- and seven-layer specimens, a 45° damage line was observed during the initial compression phase, due to the instability of the structure inducing shear deformation. As compression continued, a mixed compression and shear failure was observed. The behaviour found on five and seven-layer structures is very similar to that found on a classic metal specimen subjected to a classic metal sample

subjected to compression.

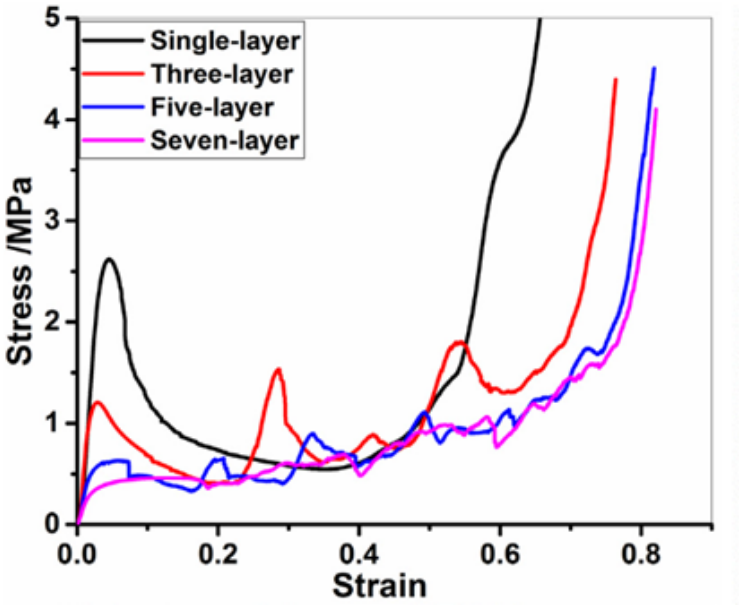

Figure 2.5: Compressive response curves of multi-layer lattice core sandwich panels: BCC. [19]

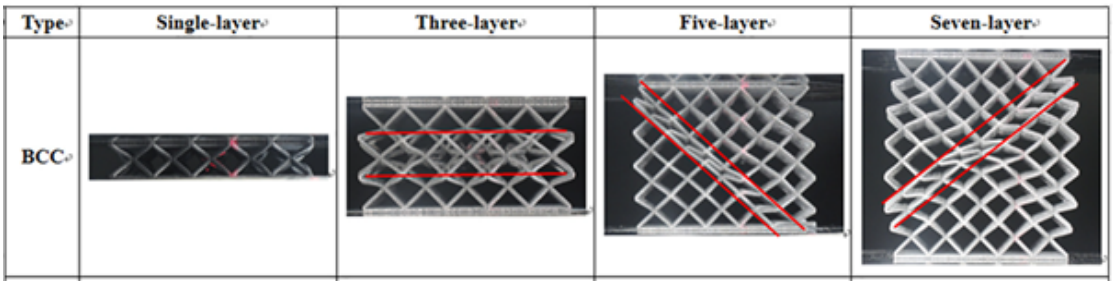

Figure 2.6: Deformation mode BCC [19]

2.2 Gibson and Ashby model

The Gibson-Ashby model is the first model to describe the performances of generic cellular material. Gibson and Ashby [7] began by correlating the mathematical equations derived from the literature with the experimental results of foam and

general cellular solids. They considered a cell structure as a classical mechanical system trying to correlate the geometrical factors whit the most important properties as the compressive Young Modulus and also the Ultimate Compressive Strength (UCS). Ashby and Gibson proposed the following relationship:

$$\frac{E^*}{E_s} = C_1 \left(\frac{\rho^*}{\rho_s} \right)^2 \tag{2.5}$$

Where E and ρ are respectively the Young modulus and the density of the material. The star values are referred to the cellular material instead of the ones the subscript 's' are referred to as bulk material. As you may notice, there is a proportionality between the RD and elastic modulus. The constant of proportionality C_1 has been established both by the experiment and by the numerical computation and it is assumed to be equal to 1 [7]. Its value can be slightly affected by the cell shape and therefore considering the cell as a bending or stretch dominated structure. The other relevant relation correlates the RD with the yield strength (or Ultimate Compressive Strength) of the cellular structure.

$$\frac{\sigma^*}{\sigma_s} = C_2 \left(\frac{\rho^*}{\rho_s} \right)^{\frac{3}{2}} \tag{2.6}$$

Even in this case there is a constant of proportionality whose value has been e established by a numerical computation and for Gibson, its value is approximately 0.3 but the value, in this case, can easily change depending on the cell type. A better summary of the formulas is reported in Table 2.1 with the correct distinction between cell response types. To better understand the relation between the relative density, Elastic modulus and UCS, it is better to have a look at Figure 2.7 where these kinds of relationships are graphically summarized. In the graph is possible to locate the macro area within which some kind of material lies.

The two dashed lines represent the equations in Table 2.1. That is the ideal behaviour of the structures. It is possible to notice that foam is represented by a big area, this is due to how they are made. Their structure is not homogeneous, the position of voids are not predictable and not equally spaced. For this reason, is not possible to create a realistic model and mechanical properties change in a very large range.

Some discrepancies between experimental results and the model's predictions have also been observed [20]. These kinds of differences depend on several factors such as:

- Residual stresses of the SLM manufactured lattice structures and roughness of the strut surfaces [2].
- The differences between the lattice density measured by Archimedes' method and SLM-fabricated components [20]. This difference is due to some unmelted powder attached to the surface producing dissimilarities with the expected results [21].
- Minimal variations in the fabricated cross-sectional areas, which lead to weak sections resisting under compression [22].

Gibson-Ashby model formulae		
Response type	**Mechanical property**	**Formula**
Bending-dominated	Modulus (E)	$\frac{E^*}{E_s} = C\left(\frac{\rho^*}{\rho_s}\right)^2$
	Strength (σ)	$\frac{\sigma^*}{\sigma_s} = C\left(\frac{\rho^*}{\rho_s}\right)^{3/2}$
Stretch-dominated	Modulus (E)	$\frac{E^*}{E_s} = C\left(\frac{\rho^*}{\rho_s}\right)$
	Strength (σ)	$\frac{\sigma^*}{\sigma_s} = C\left(\frac{\rho^*}{\rho_s}\right)$

Table 2.1: Gibson-Ashby model formulae

In conclusion, it is possible to state that the comparisons between numerical and experimental results showed a better prediction of Young modulus at high relative

density. For lattice structures with a low porosity content, the model responds more accurately.

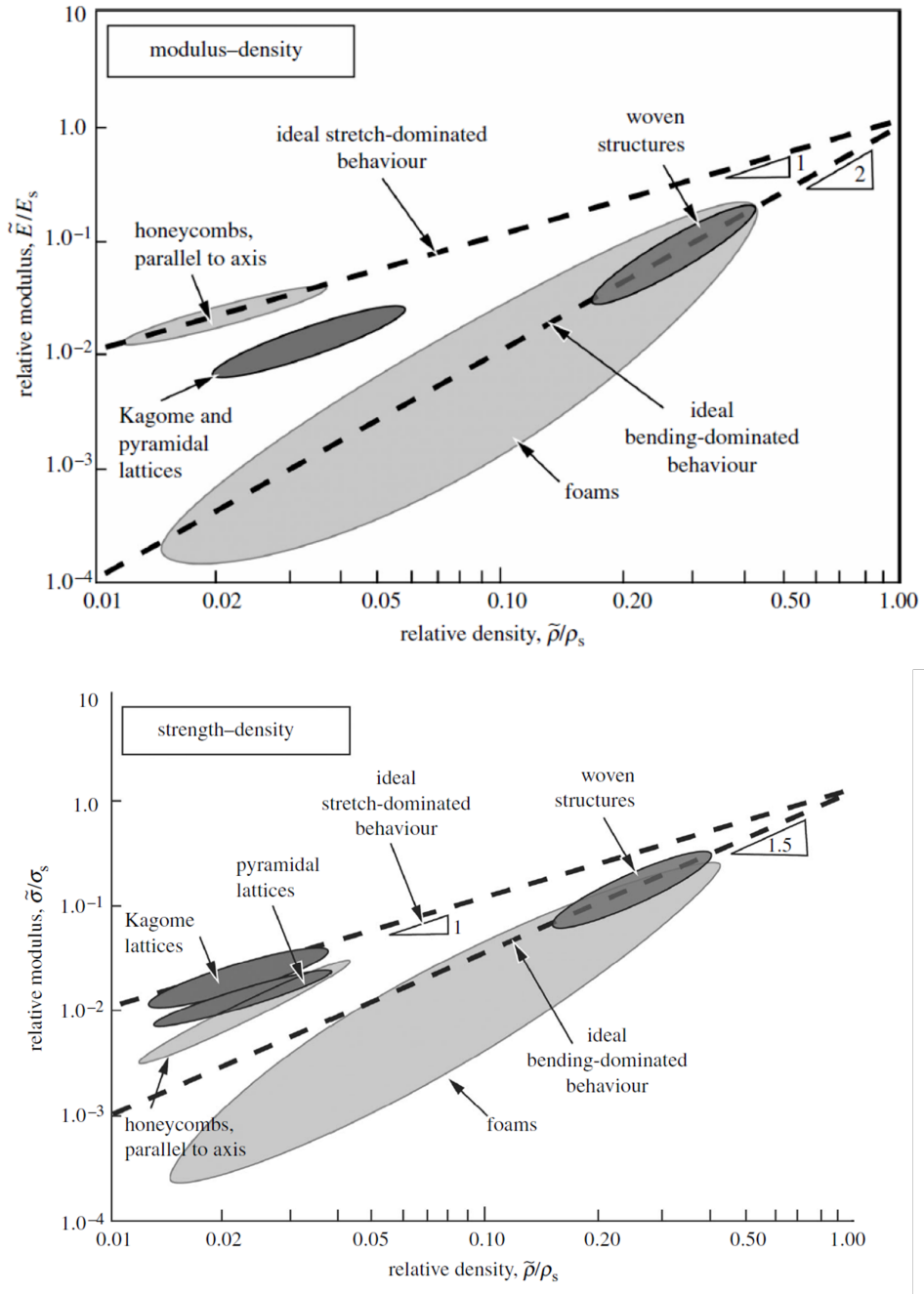

Figure 2.7: Relation between the relative density with the elastic modulus and the relative density with the yield stregnht [7]

2.3 Strut based cellular structures

The properties and deformation behaviour of lattice structures depend not only on their relative density but also on their micro-architecture and so on geometry, for this reason, nowadays different kinds of lattice structures are deeply designed and tested. It is possible to define, in the literature, a large range of strut-based lattice structures. The most common strut-based cell topologies that have been investigated are the body-centred cubic (BCC) and the face-centred cubic (FCC). The BCC lattice is characterized by rods inside the body linking the vertices while the FCC has rods linking the vertices but along the external faces. The BCC is not an optimal geometry but has the advantages of being reliable to manufacture and of having simple failure modes during uniaxial and multiaxial compression [23]. From these two more complex shapes are derived such as those with the inclusion of z-strut. If some rods are added in the z-direction, it is possible to have the BCC-Z or FCC-Z lattice structure. Other configurations are derived and are named after analogous crystalline structures. Other strut based topologies also exist, such as the diamond, octet truss, truncated cuboctahedron and rhombic. The advantage of additive is that it is very easy to create previously impossible geometries. The difficulty of the structures is not a parameter that affects production in the same way as in traditional machining where it is often a limitation. In Table 2.2 is possible to see the figure and names of different kinds of cells. There are also some references to papers that have studied that type of cell.

As strut based cellular structures are composed of struts inside, geometry lends itself to study and modelling with numerical model type tools. This is why they were among the first cells to be studied and are still used today as a reference point for more complex studies. From these basic geometries, certain modifications have been made to improve the mechanical properties. An example is Osman et al. [24], studying the behaviour of cell Octet truss but changing the aspect ratio by increasing the height of the structure in relation to its width. In the same report, he studies how hybrid composite structures, with the same geometries, exhibit very high mechanical properties with respect to the original configuration. Another example is the scientific work of Cao et al. [25] which studies how the properties of

the structure Rhombic change by modifying the cross-section area of the internal struts. Cao inputs a parameter of shape and studies how the variation of this parameter affects the behaviour of the cell. In conclusion, is possible to state that the dynamic compressive behaviour of the Rhombic samples was significantly affected by different shape parameter α values. All these works show how even starting from quite simple geometries, by modifying some form factors or changing some simple characteristics, it is possible to obtain a specimen with characteristics very different from the initial one.

Cell name	**Images**	**References**
BCC	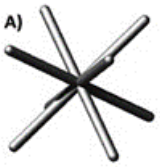	[3] [15] [14] [35] [39]
BCCZ		[14] [35] [47]
DIAMOND	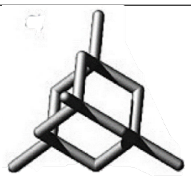	[49]
FCC	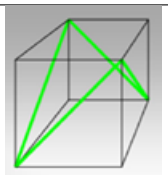	[18] [24] [50]

FCC-Z	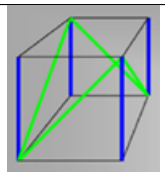	[50]
OCTET TRUSS	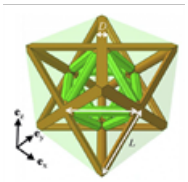	[15] [24] [38] [43]
TRUNCATED CUBOCTAHEDRON	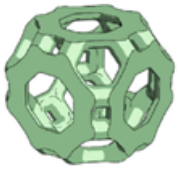	[51]
KELVIN	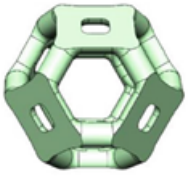	[51]
RHOMBIC		[25] [51]
HONEYCOMB	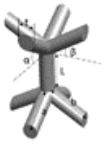	[2]

Table 2.2: A summary of Strut based cellular structures.

2.4 Triply periodic minimal surface cellular structures

Recently, an increasing amount of interest has been focused on nature-inspired triply periodic minimal surface (TPMS) structures. TPMS are minimal surfaces, which are a subset of hyperbolic surfaces [26]. A hyperbolic surface is a surface composed of hyperbolic geometry which is, in mathematics, a non-Euclidean geometry. The main difference between a surface in hyperbolic geometry and normal Euclidean geometry is that in hyperbolic geometry there are at least two distinct lines that pass through a given point and are parallel to a given line. Instead, an Euclidean geometry has exactly one line through a given point in the same plane as a given line which is never intersected. Lagrange (1760) was the first to try to solve the problem of finding the surface that forms the smallest area for a given perimeter, in this way the study of minimum surfaces originated. In mathematics indeed a minimal surface is a surface that locally minimizes its area. This is equivalent to having zero mean curvature.

TPMS are defined as minimal surfaces that are infinitely periodic in all three independent directions, without self-intersections and partitioning the space into two labyrinths. There are several methods to generate mathematically this surface. Examples are parametric, implicit or boundary methods. The implicit method uses a single-valued function Φ of three variables to define the surface. It is represented by the locus of points such that the function has some constant value $\Phi = c$. The 3D models of the TMPS geometries were created by extracting the zero level-set surface, so imposing $\Phi = 0$. Some examples to describe the surfaces are represented by the following nodal equations (to the first order of approximation):

$$\Phi_P(x, y, z) = \cos(\omega x) + \cos(\omega y) + \cos(\omega z) = c \tag{2.7}$$

$$\begin{aligned}\Phi_D(x, y, z) = &\sin(\omega x)\sin(\omega y)\sin(\omega z) + \cos(\omega x)\sin(\omega y)\sin(\omega z) + \\ &+ \sin(\omega x)\cos(\omega y)\sin(\omega z) + \sin(\omega x)\sin(\omega y)\cos(\omega z) = c\end{aligned} \tag{2.8}$$

$$\Phi_G(x,y,z) = \cos(\omega x)\sin(\omega y) + \cos(\omega y)\sin(\omega z) + \cos(\omega z)\sin(\omega x) = c \quad (2.9)$$

$$\begin{aligned}\Phi_{IWP}(x,y,z) =& 2[\cos(\omega x)\cos(\omega y) + \cos(yx)\cos(\omega z) + \cos(\omega z)\cos(\omega x)] + \\ &- [\cos(2\omega x) + \cos(2\omega y) + \cos(2\omega z)] = c\end{aligned} \quad (2.10)$$

where (x, y, z) represent the special coordinate, $\omega = \frac{2\pi}{l}$ and l is the length of the unit cell. The subscripts P, D, G and IWP refer respectively to the Primitive (Φ_P), Diamond (Φ_D), Gyroid (Φ_G) and IWP (Φ_{IWP}). In Table 2.3 figures of some TPMS structures are reported.

In terms of manufacturability, the TPMS structure has self-supported features that do not require the building of support structures and this kind of feature is suitable for being fabricated by SLM technology.

The Gyroid is one of the most studied types of triply periodic minimal surfaces and it was discovered in the 1970s by NASA (National Aeronautics and Space Administration) scientist Alan Schoen. Even if this kind of structure is present in nature, such as the microstructure of butterfly wings.

The advantages are:

- The structure is connectable and can easy exclude powder or liquid resin when manufactured by AM.
- Its spiral structure has a self-supporting capability during the manufacturing process by AM.
- Its structure has high specific strength at low density.
- Compered to strut-based lattice structures, TPMS-sheets don't need joints and struts, so they might have significant advantages regarding manufacturing and effective properties of the cellular material [27].

Cell name	Images	References
SCHWARZ DIAMOND	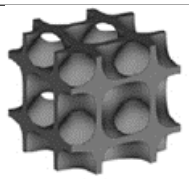	[20] [28] [32]
SCHWARZ PRIMITIVE	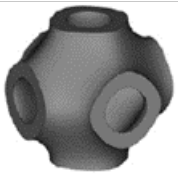	[25] [51]
SCHOEN GYROID	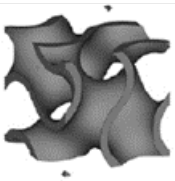	[20] [28] [32] [36] [43]
SCHOEN IWP	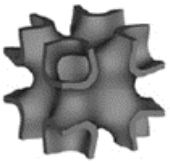	[43]

Table 2.3: A summary of TPMS cellular structures.

Studies also suggest the curvature of implant surfaces plays a critical role in promoting bone ingrowth [17], TPMS lattice structures potentially offer improved Osseo-fixation over strut-based lattice structures [28]

2.5 Other types of unit cells

Academic literature shows that there are other types of solutions to obtain lattice structures. A possible alternative is unit cells based on topology optimisation. Starting from certain load conditions and specific constraints, unit cells can be optimised to obtain specific performance requirements. By optimising unit cell

struts' size (i.e. thickness, length and diameter) and geometries it is possible to realize a good compromise between customisation of the product and lattice structures with specific performances [18][29]. The possibility of creating any type of geometry has made it possible to create structures also with a negative Poisson's coefficient. All the structures illustrated so far belong to the category of uniform structures. There is in the literature a wide range of structures that are not uniform. These non-uniform structures make the designer realise more free design to meet the needs of specific applications. Non-uniform structures include gradient and stochastic ones. They are structures very common also in nature and don't have uniform density but the porosity is variable throughout the structure. This particularity allows these types of structures to have different characteristics from classic structures.

Wang et al. [30] investigate the design and the mechanical behaviour of structure gradient distribution of porosity. This type of structure is widely used especially in the biomedical field where it is possible to build artificial bones with graduated porosity. Thanks to their internal structure very similar to that of the bones, it is possible to create artificial bones very light and with good mechanical characteristics. The geometry was realized according to the Voronoi-Tessellation method of space partition. In Figure 2.8 is possible to see the final porous scaffold design with a gradient along the z-axis.

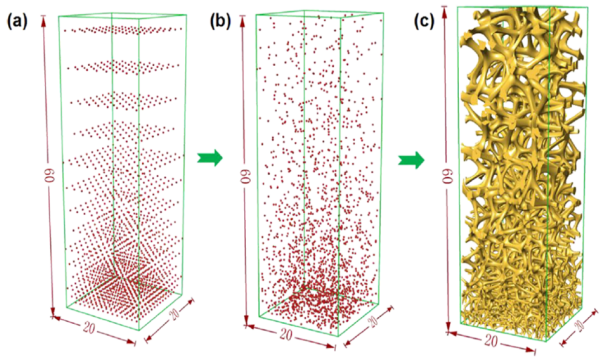

Figure 2.8: Modelling method of porous scaffold with gradient porosity. (a) Regular lattice. (b) Irregular lattices. (c) Porous scaffolds with gradient distribution of porosity (Kt = 0.9, Kb = 0.7). [30]

Wang et al. stated that the mechanical behaviour of the gradient pore structures is significantly different from uniform porous structures in the platform stage. The compressive stress platform of the gradient pore structure tends to rise. The larger the porosity gradient, the larger the angle of ascent. Is possible to see the curves in Figure 2.9.

On the other hand, stochastic structures are very often generated by mathematical functions. it is not possible to recognise a unit cell within them as they can be very irregular. Ibrahim et al. [2] studying the behaviour of stochastic versus regular lattice structure stated that the regular one exhibit a higher stiffness in the elastic region than the stochastic one. It is possible to assert that the regular lattice shows lower energy storage as well throughout the elastic region.

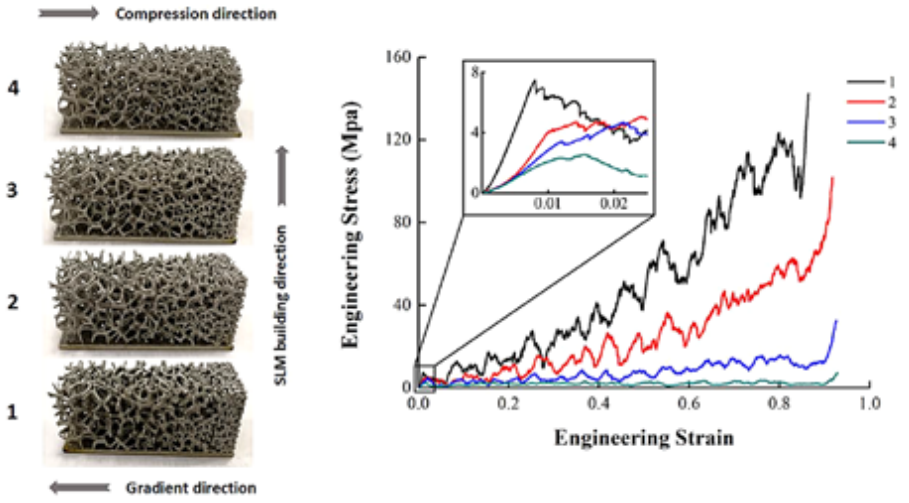

Figure 2.9: Gradient pore structure and compressive test curve [30].

2.6 Data collection

After the literature search and filtering, metal AM lattice structure data were summarised in Table 2.4. The references, unit cell topology, material, and the type of data collected from the paper are also present in the table. The properties are abbreviated as compressive elastic modulus (EC), yield stress (YS), Poisson's ratio

Author	Unit Cell Topology	Test Type	Property	Data Type	Material
Cao [25]	Rhombic dodecahedron	Quasi-static compression tests	EC, YS, SEA	E, F	SS 316L
Zhang [32]	BCC, TPMS Gyroid, TPMS Primitive, TPMS Diamond	Compression tests	EC, YS, SEA	E, F	SS 316L
Gümrük [33]	BCC	Tensile test, Compression tests	EC, YS	E, F	SS 316L
McKown [34]	BCC, BCCZ	Compression tests	EC, YS, PR	E	SS 316L
Shen [14]	BCC, BCCZ	Compression Tests, Three-point Bend Tests	YS	E	SS 316L
Xiao [18]	FCC, VC, ECC	Compression tests	EC	E	SS 316L
Smith [35]	BCC, BCCZ	Quasi-static Compression tests	EC, YS, PS	E, F	SS 316L
Yan [36]	TPMS Gyroid	Compression tests	EC, YS	E	SS 316L
Yan [37]	TPMS Gyroid	Compression tests	EC, YS	E	SS 316L
Ushijima [23]	BCC	Compression tests	EC, PR	A, F	SS 316L
Tancogne-Dejean [38]	Octet-Truss		EC, PR	F	SS 316L
Tsopanos [31]	BCC	Compression test	EC, YS	E	SS 316L
Osman [24]	Octet truss lattice (OTL), FCC with different ratio	Static compression, Dynamic compression	YS	E	SS 316L
Guo [39]	BCC	Quasi-static compression tests		F,E	SS 316L

Table 2.4: A summary of analysed work

(PR) and plateau stress (PS). The data types are abbreviated as analytical (A), FEA(F), and experimental (E). The conclusions of some scientific papers are then reported in order to illustrate some of the properties of these structures just described.

Osman et al. [24] analysed the compressive behaviour of the FCC lattice structure in comparison with the same geometry cell but doubling the ratio between the length and the height of the base cell. And it was shown that the yield strength of the new configuration is more or less 80% higher than the classical configuration fabricated with the same material and the same relative density. It was confirmed both numerically and experimentally. Tsopanos et al. [31] studied how laser power influences the mechanical property of the BCC lattice structure. The study's conclusion states that for low laser power settings (less than 80 W) considering as constant exposure time the porosity increase and so there was a 50% drop in material strength from the stainless steel 316L bulk values. Guo et al. [39] analysed how the struts aspect ratio of the BCC lattice structure can increase the accuracy of the model. Yan et al. [36] evaluated the mechanical properties (Yield strength and compression modulus) of gyroid lattice structures with various unit cell sizes. They have observed that both the characteristics were considerably decreased with increasing unit cells. This is due to the fact that the strut density of the gyroid lattice structures decreases with increasing unit cell size. Li et al. [40], studied how the anisotropy of density varies in the gyroid structure. The spatial arrangement of the unit materials deeply affects the elastic anisotropy of the cellular structure. Although the gyroid cellular structure is not easy to see symmetry in geometry, it can be seen from the analysis of the anisotropic that it belongs to the form of the cubic crystal system. Moreover, it can be seen from the results (Figure 2.10) that the sheet-based gyroid cellular structure is similar to isotropic at both low-density and high-density, while the strut-based gyroid structure has obvious anisotropy. Additionally, the sheet-based gyroid structure has a higher Young's modulus than the strut-based gyroid structure at the same density. In theory, anisotropic structures are not conducive to energy absorption

Ma et al. [41] analysed the mechanical properties of 316L gyroid structures stating that were suitable to be designed as bone scaffolds in terms of mechanical

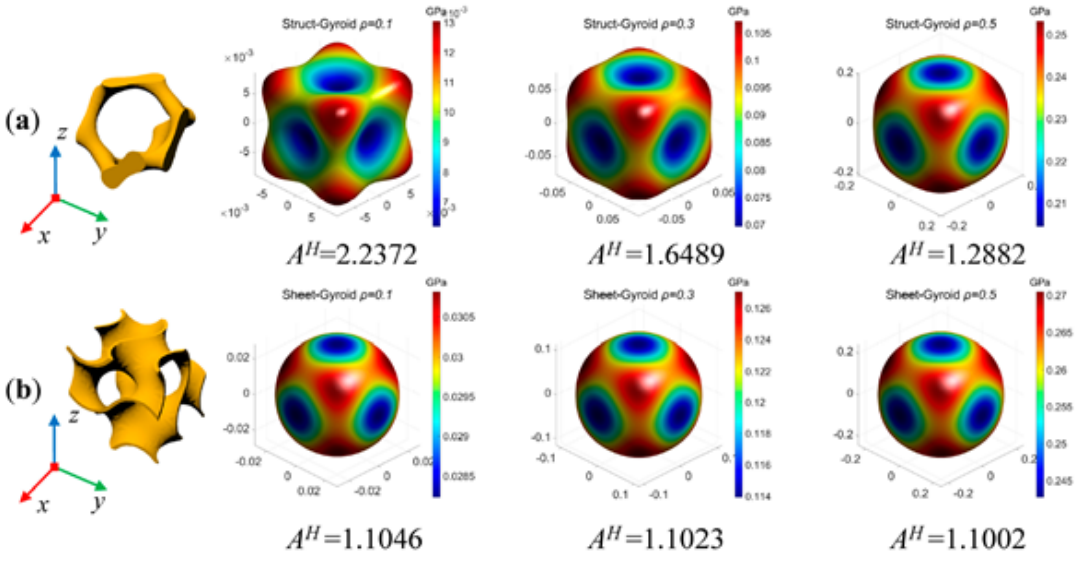

Figure 2.10: Anisotropy of strut-based gyroid (a) and sheet-based gyroid (b). (If AH is close to unity, the structure could be treated as isotropic). [40]

properties and mass transport properties. In addition by changing the porosity, it is possible to get the bone scaffolds with similar elastic moduli and yield strength to human bone. In this way is possible to avoid stress shielding and implant failure [41]. Regarding CFD analysis the structure exhibit good flow performance, with almost no turbulence.

2.6.1 Energy absorption

Zhang et al. [32] analysed the energy absorption behaviour and applications of lattice structures. Zhang says that the deformation of TPMS sheet structures thanks to the high plateau stress and high densification rate is suitable for energy absorption applications. In this kind of implementation, it is generally required a high amount of energy absorbed per unit volume as well as the corresponding maximum stress. The diagram in Figure 2.11 shows the performance under a constant strain rate (corresponding to quasi-static loading). An energy-efficient structure gives a high envelope and a scale of density located at the top right corner. The diagram indicates that the TPMS sheet structures outperform BCC

lattice in energy absorption, namely with the same allowable stress, TPMS sheet structures can absorb more energy. Zhang et al. also state that the D-sheet (Diamond) structures exhibit superior energy absorption abilities as their density scales are approaching the upper right corner, which may be interpreted as D-sheet structures requiring lower densities to achieve the same allowable stress and energy per volume.

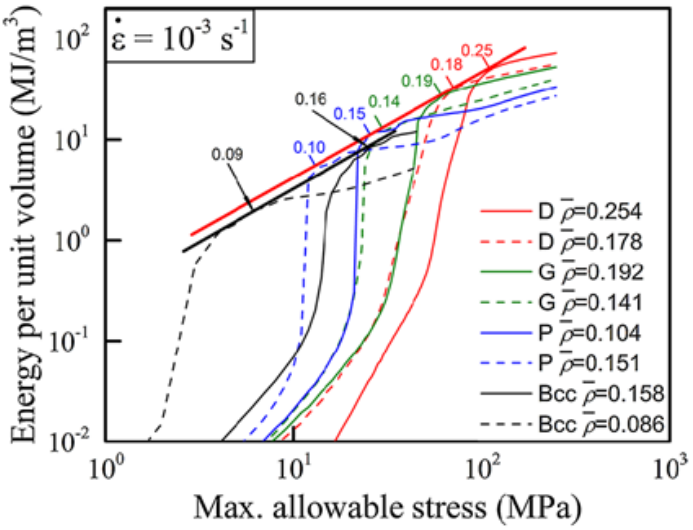

Figure 2.11: Energy absorption diagram of TPMS sheet structures and BCC lattices. [32

2.6.2 Fatigue performances

Understanding the fatigue behaviour of mechanical components is quite an important aspect for lots of applications (e.g. aerospace industry), for this reason also some tests with dynamic load were performed. Although the structure of the open-cell and closed-cell foam is different, three different steps could be observed in their fatigue failure. In the first step, within a few cycles, the strain increases rapidly. In the second step, the accumulative strain does not change significantly. This step takes 104–106 cycles. In the third step, cumulative strain raises exponentially, which eventually causes failure of the specimen in a few cycles. In most cases, the

fatigue experiments were performed under fully compressive loading and the ratio of maximum to minimum load is about 0.1 to ensure that the specimens remain in their place during the test [42]. The factors that influence fatigue properties of lattice structures are:

- The bulk material's mechanical properties
- Relative density
- Cell topology
- The geometry of the cell struts, that define the distribution of material inside the cell

Lattice fatigue life has been found to consistently increase with increased relative density, but cell topology significantly affects fatigue results [17]. As it is possible to see from Figure 2.12, both relative density and topology affect lattice structures fatigue performances. Lattice structures with grater RD could sustain grater loads for a large number of cycles than those with lower relative density. But from Figure 2.12, it is possible to state that truncated cuboctahedron lattice structures could sustain greater loads for similar periods than diamond lattice structures whit similar relative densities. It is also possible to say that manufacturing defects as the staircase effect can significantly affect the fatigue properties.

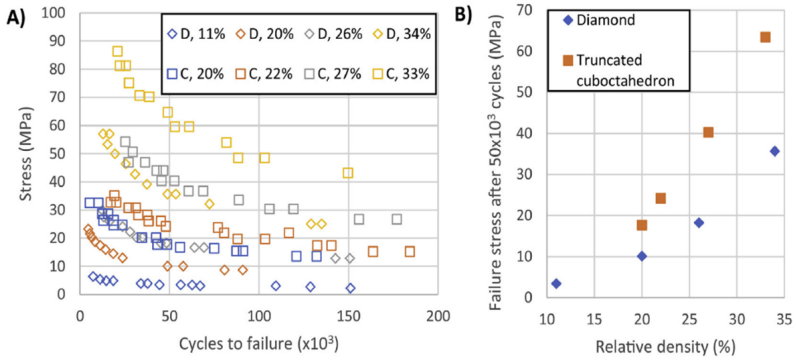

Figure 2.12: Comparison of fatigue behaviour of SLM lattice structures with diamond (D) and truncated cuboctahedron (C) topologies and varying relative densities (%). B: Failure stress after 50 x 10^3 cycles for different topologies and relative densities [17]

2.6.3 Thermal and electrical conductivity

Another important aspect is the thermal and electrical behaviour of these structures. In Figure 2.13 is illustrated the variation of the effective electrical/thermal conductivity when the relative density of the structures is varied. The effective electrical/thermal conductivities of the foams are normalized with the electrical/thermal conductivity of the base material. In this way, $\frac{k^*}{k_s}$ implies the percentage of capturing the electrical/thermal conductivity of the base material by the different TPMS at different relative densities Figure 2.13 shows that the effective conductivities of the Primitive, IWP, Neovius, and Gyroid are very close to each other. Note that these kinds of structures have cubic symmetry, so only one value is required to describe their electrical/thermal conductivity tensor [43].

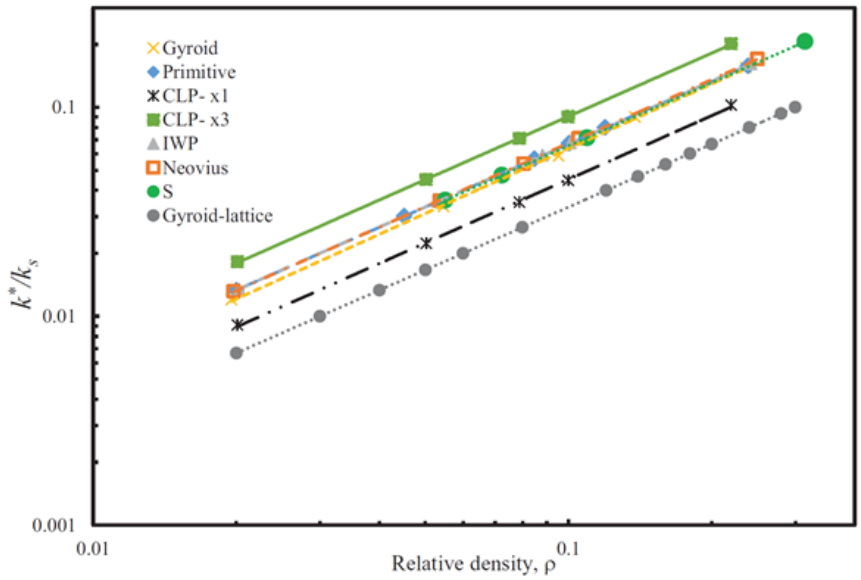

Figure 2.13: Electrical/thermal conductivity of TPMS-foams at varying relative density. [43]

2.6.4 Acoustic properties

During past years lattice structures have been investigated also under the acoustic field. Sun et al. [44] analysed sound insulation and sound absorption of a different

kind of lattice structure. The conclusion of the work stated that the microstructure of the structure was not the main parameter affecting the properties. Instead, the differences in porosity and pore size in the cell were the main reason for the differences in acoustic properties. The structure exhibit excellent sound insulation properties in the range of 1 kHz and 5 kHz as it's possible to see in Figure 2.14. Regarding sound absorption properties, some kinds of structure were better than those of the bulk material in the range 1 kHz and 6.3 kHz as is possible to notice in the Figure 2.14.

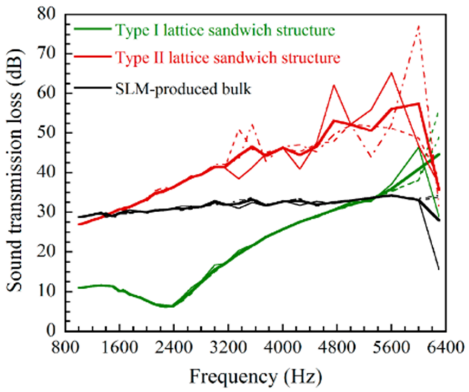

Figure 8. Sound insulation property curves of the three different structural acoustic specimens. (The thin line curves and dotted line curves in this figure are the octave spectrums of each group of sound insulation property test. The three heavy line curves in this figure are the average value curves of the octave spectrums of the three structures).

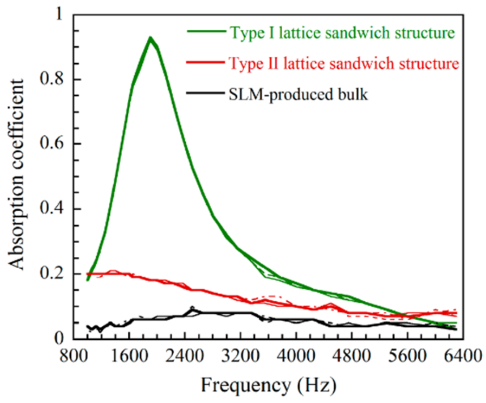

Figure 9. Sound absorption property curves of the three different structural acoustic specimens. (The thin line curves and dotted line curves in this figure are the octave spectrums of each group of sound absorption property test. The three heavy line curves in this figure are the average value curves of the octave spectrums of the three structures).

Figure 2.14: Figure taken from [44]

2.6.5 Comparison between reported experimental data and predictions of the Gibson-Ashby model

As stated before, the Gibson-Ashby model relates the relative density $\left(\frac{\rho^*}{\rho_s}\right)$ with the relative modulus $\left(\frac{E^*}{E_s}\right)$ or strength $\left(\frac{\sigma^*}{\sigma_s}\right)$ of a lattice structure material. The equations of Table 2.1 show dependency from a coefficient C and un exponent n. These coefficients are usually derived experimentally but it is possible to identify a range of maximum and minimum values to locate the values. The Gibson-Ashby model predicts the coefficients for metallic open-celled cellular structures to be in the range [0.1 - 4] and [0.1 - 1] for modulus and strength respectively [17]. As noted earlier, the data were normalised by dividing the reported property value of the lattice structure by the bulk mechanical property of the constructed material.

Collecting data from a certain number of scientific papers is possible to plot all the values in a graph as reported in Figure 2.15.

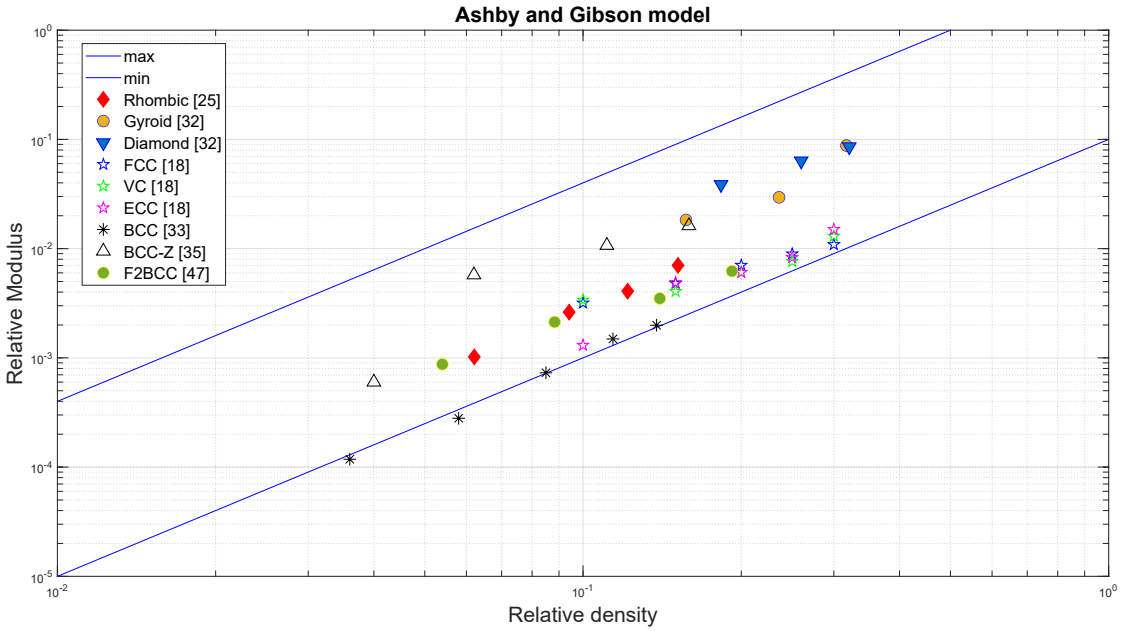

Figure 2.15: Comparison of reported experimental modulus data with the predictions of the Gibson-Ashby model

From the comparison is possible to notice that:

- Almost all the values fall within the predicted range for the modulus
- Consistent with the finding of McKoen et al. the moduli of BCC lattice structures were found to be in the lower range or below the predicted range

2.7 Numerical Simulation Theory

A different approach to predicting the behaviour of solid lattices is based on simulation. There are different kinds of simulation models; some of them rely on statistical methods, semi-analytical, or fully numerical methods. The Finite Element Method (FEM) is a powerful mathematical tool that is employed for the prediction of the mechanical response of the structures. It is based on the approximation of the behaviour of a continuum by subdividing it into many simple solid elements (so-called Finite Elements) that approximate the local behaviour of the system. It is certainly possible to obtain models with high accuracy that simulate well various deformations and stresses locally. At the same time, they require meshing the entire structure and this can be very challenging and certainly time-consuming because the accuracy is related to the quality of the mesh generated. These models require a lot of computational power because the generated files are very large. However, as the complexity of the geometry increases, the computational effort grows and becomes difficult to sustain. This particularly holds for lattices where the number of elements scales up with n^3.

It is possible in this case to use a different approach that aims to treat the material as an infinite medium. The study of the microscopic behaviour of the unit cell leads to defining the behaviour at the macroscopic level. This process is called homogenization. Making use of homogenization, lattices mesoscopic properties are linked with a medium, used in simulations as a bulk material [45]. Geometrical periodicity and periodicity in boundary conditions ensure that the microscopic

properties can be extended to all the volume filled by the lattice (theoretically infinite). The aim of homogenization is the reduction of the number of degrees of freedom (DOF) in the mechanical model, from the displacements and rotations of the countless individual micro-structural members to a much smaller number of macroscopic displacements and rotations.

Homogenization models are for sure dependent on how more or less accurate the microstructure/mesostructure model the method is based on is well structured. These methods have been originally developed for composite materials [46]. This process generates a linear orthotropic medium material whose properties are defined through linear static simulations for compression/traction and shear in the main principal directions. Once the stiffness matrix of the material is defined via simulations outputs, this is used to obtain the moduli needed for the definition of the orthotropic material.

2.7.1 Homogenization

As mentioned above, it is possible to treat the effective physical behaviour of lattice structures on the macroscopic level as a homogenized pseudo-material. But the behavior of cellular structures on the macroscopic level is certainly governed by the physical process on the microscopic level, where the behavior of individual strut or cell walls has to be observed or predicted. An equivalent Young's Modulus and Shear Modulus can be assigned for each principal direction. The core idea behind homogenization is to take a periodic unit cell representative of the repetitive structure and apply some periodicity boundary conditions. If a bidimensional model (2D) is taken into account, is possible to consider that the unit cell is contained in a rectangular area with four nodal vertex and four edges. It is possible to define the undeformed and a deformed configuration of the original rectangle as shown in the Figure 2.16. Referring to Figure 2.16 the boundary consists of four edges (identified by the letter N, S, W, and E)

The rectangular region has to be constrained against rigid body motions modes: on one hand, corner node SW is contained to suppress rigid body translations

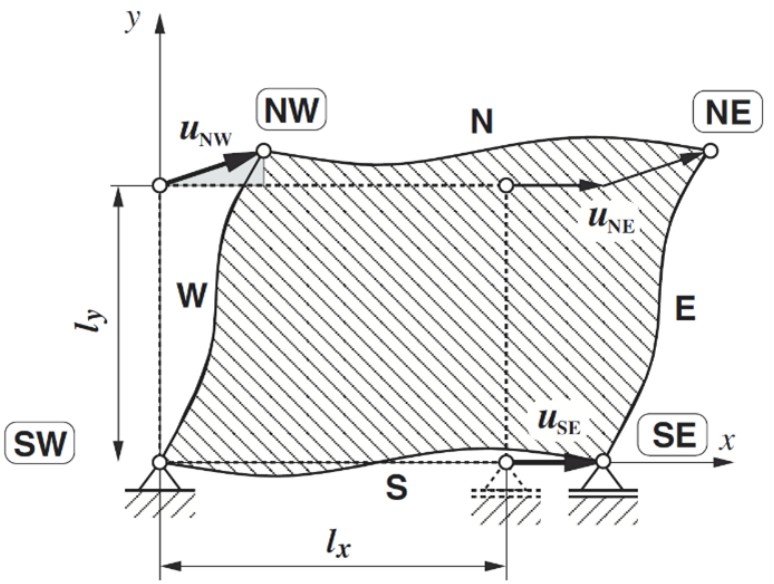

Figure 2.16: Idealized 2D unit cell in the undeformed and a deformed configuration. Dispacemnt vectors and letter codes are given for eache corner and edge nodes. Single letter codes denote edges, two letter codes denote corners. [45]

and on the other hand the vertical displacement component of the finite element nose SE is constrained to prevent a rigid body rotation. But the unit cell can still deform. To guarantee the geometrical periodicity also in the deformed state of the unit cell, the displacements of opposite boundary edges have to be coupled. The DOFs of one of these coupled edges remain unconstrained. For this reason, edges S and W are called "master" DOF, while N and E are called "slave" edges. The choice of master and slave entities is arbitrary and does not change the final result, but it must be coherent in all the calculations. The components of these displacements are related to the macroscopic strain tensor which is described in vector notation by the vector of its component $\epsilon = \{\epsilon_{xx}, \epsilon_{yy}, \gamma_{xy}\}$ where:

$$\epsilon_{xx} = \frac{u_{SE}}{l_x} \qquad \epsilon_{yy} = \frac{u_{NW}}{l_y} \qquad \gamma_{xy} = \frac{u_{NW}}{l_y}$$

The horizontal DOF of the node SE il is related to the macroscopic normal strain in the y-direction while the horizontal and vertical displacements of the corner nose SW define the macroscopic shear strain and the macroscopic normal strain in the y-direction. The displacement of the edges N and E are connected with the nodes

at the opposite edges (S e W) and the following equations hold:

$$u_E(y) = u_W(y) + u_{SE}$$
$$u_N(y) = u_S(x) + u_{NW}$$

The displacement vector of the corner node NE, on the other hand, is a linear combination of the displacement vector u_{NW} and u_{SE}:

$$u_{NE} = u_{NW} + u_{SE}$$

Since the displacements of all nodes on the slave edges are coupled to master nodes, the forces acting on the master nodes are distributed over the entire edges and the stresses are summed up until static equilibrium is reached. The unit cell model reacts to concentrated loads in the same way an infinite periodic structure would react to homogenized applied stress. So it is possible to establish a relationship between the homogenized stress state $\sigma = \{\sigma_{xx}, \sigma_{yy}, \sigma_{xy}\}$ and the concentrated horizontal and vertical nodal forces H and V. The resultant forces are divided by the edge length to obtain the mean stresses:

$$\sigma_{xx} = \frac{H_{SE}}{l_y} \qquad \sigma_{yy} = \frac{V_{NW}}{l_x} \qquad \sigma_{xy} = \frac{H_{NW}}{l_x}$$

At this stage, knowing the strains and stresses is possible to calculate the elasticity matrix [E] which contains the characteristics of the homogenized material. Below is the equation (2.11) that governs the physics of the phenomenon

$$\begin{bmatrix} \epsilon_{xx} \\ \epsilon_{yy} \\ \gamma_{xy} \end{bmatrix} = \begin{bmatrix} \frac{1}{E_{xx}} & -\frac{\nu_{yx}}{E_{yy}} & 0 \\ -\frac{\nu_{yx}}{E_{xx}} & \frac{1}{E_{yy}} & 0 \\ 0 & 0 & \frac{1}{2G_{xy}} \end{bmatrix} \begin{bmatrix} \sigma_{xx} \\ \sigma_{yy} \\ \sigma_{xy} \end{bmatrix} \tag{2.11}$$

The elasticity matrix can be used inside the simulation phase and it is specific for one type of lattice structure. It is representative of the characteristic of the lattice. Of course in a 3D case, the elasticity matrix will be a 6x6 matrice. This equivalent material is also used in FE simulations treating the lattice as a solid region, thus reducing greatly the number of elements.

Thanks to homogenization it is possible to get some information in the fastest and easy way. Even if the results are less accurate and we are not able to detect the edge effect or the stress concentration, homogenization is a powerful tool when the objective is to compare different lattice types. It is a powerful tool when to investigate how a change in the unit cell affects the global behavior of our geometry.

3 Materials and Methods

3.1 Design of the experiments

In this study, the behaviour of three different unit cell topologies has been analysed (Figure 3.1):

1. Structure I: Dode Thick
2. Structure II: Dode Medium
3. Structure III: Gyroid

Structures I and II have been designed using Magics while the Gyroid structure has been designed using nTopology. The generic specimen has a cubic volume with a length equal to 15 mm.

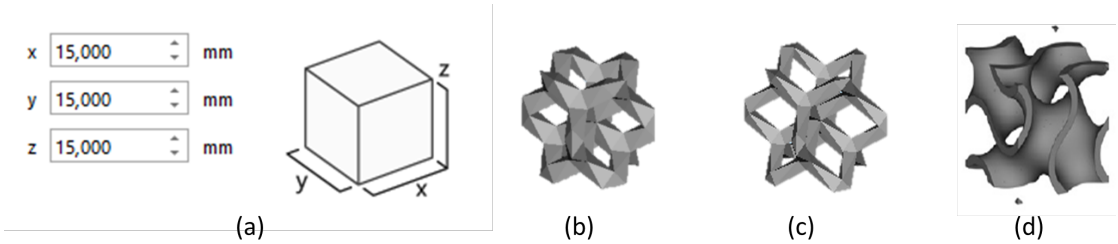

Figure 3.1: (a) Volume of the structure (b) Dode Thick unit cell (c) Dode Medium unit cell (d) Gyroid unit cell

For each topology it was decided to vary the size of the unit cell, starting from 4 mm and moving to 6 mm and 8 mm. The size of the cell is modified to vary the internal design of the cell and thus its relative density. All other parameters such

as surface shape and thickness (case of Gyroid structure) are left unchanged. Three different layouts were then made for each topology, for a total of 9 configurations. All the different configurations are reported in Figure 3.2.

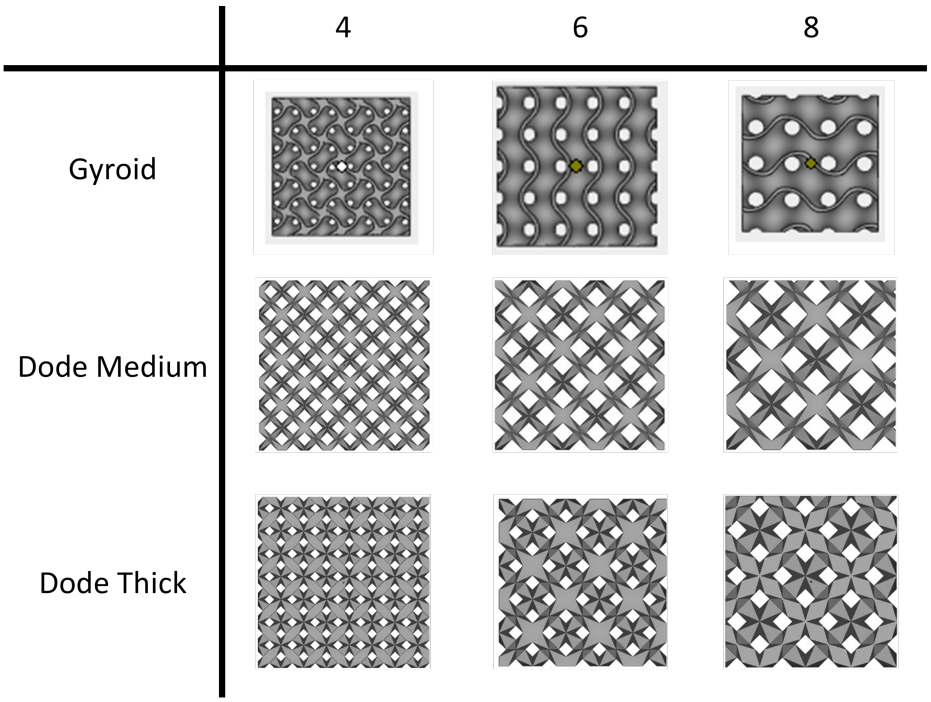

Figure 3.2: Possible configurations

3.2 Production

To make the samples, the Mlab R machine by GE Additive machine [48] has been used. This machine has a laser source with a maximum nominal power of 100 W. The working plate has dimensions 90x90x80 mm and is suitable for different kinds of applications. Once the powder has been loaded into the powder chamber, the machine is closed and the process parameters are set. Thanks to the flow of pure nitrogen, the percentage of oxygen in the chamber is kept below 0.2-0.1% to avoid any contamination during powder melting.

In order to guarantee a robust experimental analysis, three replicas have been

produced for each cell typology and size. The build job was prepared using Magics. Samples have been divided into two jobs to saturate the working plate. They have been conveniently spaced along the building plane to have a uniform temperature distribution during all the building phases. Additionally, all the samples were tilted by approximately 5 degrees to prevent any forces generated as the roller passed through. The distribution of all the samples and the partition between the two jobs is shown in Figure 3.3. The two jobs operated with the same process parameters, the DOE of both are reported in Table 3.1.

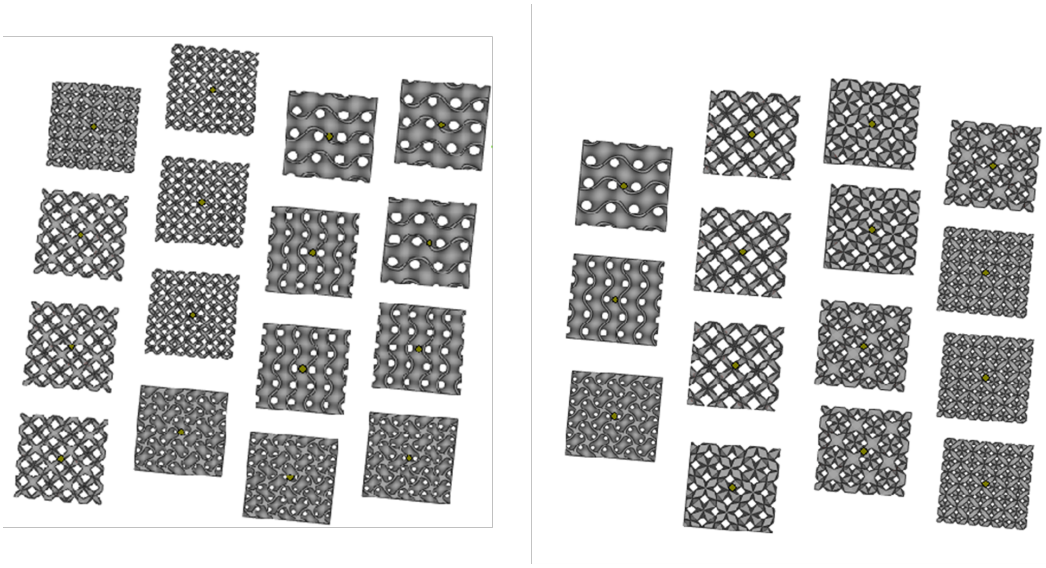

Figure 3.3: The distribution of all the samples and the partition between the two jobs.

3.3 Material

As mentioned above, the material used for the production of the specimen is the EOS StainlessSteel 316L. 316L Stainless steel is a corrosion-resistant austenitic iron-based alloy, for this reason, is suitable for a huge range of applications. From the turbine industry of aerospace to the automotive industry and lifestyle products. The chemical composition of the material is reported in Table 3.2. The powder has a granulometric distribution in the range between $15 - 50\mu m$.

	JOB 1	**JOB 2**
Number of samples	16	15
Material	SS 316L	SS 316L
Power	95 $[W]$	95 $[W]$
Scanning speed	600 $[mm/s]$	600 $[mm/s]$
Hatch distance	84 $[\mu m/s]$	84 $[\mu m/s]$
Layer Thickness	25 $[\mu m]$	25 $[\mu m]$
VED	75.4 $[J/mm^3]$	75.4 $[J/mm^3]$
Scanning strategy	Continuous exposure	Continuous exposure

Table 3.1: DOE Job 1 and Job 2

Element	**Composition** $[wt\%]$
Fe	Balance
Cr	17.00 – 19.00
Ni	13.00 – 15.00
Mo	2.25 – 3.00
C	0.030
Mn	2.00
Cu	0.5
P	0.025
S	0.010
Si	0.75
N	0.10

Table 3.2: Chemical composition

3.4 Measurements and characteristics

Once the job was completed, the platform was removed from the machine and then the specimen was removed from the building platform through an EDM wire cutting machine. To evaluate the actual relative density of each sample, mass measures were conducted and then the mean value was taken to evaluate the mass of the whole sample ($m_{lattice}$). Successively the mass of the lattice samples was

divided by its theoretical volume, evaluated as the volume of a cube of 15 mm as length. At this point was possible to derive the relative density $\left(\frac{\rho}{\rho_S}\right)$ by dividing this last calculated parameter by the density of 316L bulk material $\rho_S = 0.0079$ $\left[\frac{g}{mm^3}\right]$.

In Table 3.3 all the parameters calculated during the procedure are reported and the value of the relative density for each kind of structure. At first glance, it can be seen that the Gyroid structure has a relative density value that varies from 25% to 13% simply by changing the size of the unit cell, while the values for the Dode structures vary in a much more limited range. This is because, in the case of the Gyroid structure, the thickness of the wall surfaces has been left unchanged by changing the cell size. As far as the Dode Medium and Dode Thick structures are concerned, on the other hand, by varying the size of the base cell, the diameter of the internal struts is also varied, making the variation of volume and therefore of mass and RD very limited.

3.5 Compression tests

Uniaxial compression tests were performed in the lab of Politecnico di Torino. During the test, the lattice structure was centrally located between two plates. The bottom plate was fixed while the top plate was moved with a constant strain rate of 2 mm/min up to the densification of the collapsed lattice structure. To avoid the build orientation effect, the compression tests were conducted according to the build direction (Z direction). For the samples of the same unit cell type and size, the trends of the curves were almost similar. The behaviour expected was the one described in section 2.1. In fact, all three cells showed behaviour that can be attributed to bending dominated lattice structures. In the beginning, we have the part of elastic deformation (a) during which the compression of the specimen is very limited but the force increases rapidly, with a linear behaviour according to Hook's law. Then, having passed a certain threshold value (b), the curve flattens out, we have a long stretch in which the force remains constant (c) while the deformation continues to increase. In this phase, we can see a real compression of the specimen. Thanks to the geometry of the specimen, and the

Structure	**Cell size** $[mm]$	$m_{lattice}$ $[g]$	$\boldsymbol{\rho^*}$ $[g/mm^3]$	$\boldsymbol{\rho_s}$ $[g/mm^3]$	$\frac{\rho^*}{\rho_s}$ [%]
Gyroid	4	6.64935	0.00197	0.0079	25%
	6	4.3414	0.00129	0.0079	16%
	8	3.3888	0.00100	0.0079	13%
Dode Medium	4	3.7834	0.00112	0.0079	14%
	6	3.1793	0.00094	0.0079	12%
	8	4.0410	0.00090	0.0079	11%
Dode Thick	4	6.8496	0.00203	0.0079	26%
	6	6.3825	0.00189	0.0079	23%
	8	6.2886	0.00186	0.0079	24%

Table 3.3: Average properties of each different sample's unit cell type and size

fact that it is a bending-dominated structure, a real breakage is not reached. As explained in Chapter 2, the number of layers is very small and this favours this kind of behaviour. At this stage, the specimen can absorb a large amount of energy. Indeed this long plateau stress is very useful for energy absorption because the structure is deforming without breaking or increasing the load. After this stretch, we can observe the densification (d) zone. In this phase, the faces of the various surfaces begin to come into contact and this leads to a rapid increase in the force acting on the specimen and to real compaction of the specimen. At approximately 70% deformation, the test was considered complete (e). The machine was stopped because the data of the next part was not needed. The test specimen was then removed and the data stored in memory. All the deformation mechanisms of the lattice structures can be observed in Figure 3.4. Among the data recorded by the machine is the time, the position of the upper plate and thus the deformation and

the force applied. With this data, it was possible to plot Force vs Displacement graphs for each cell type.

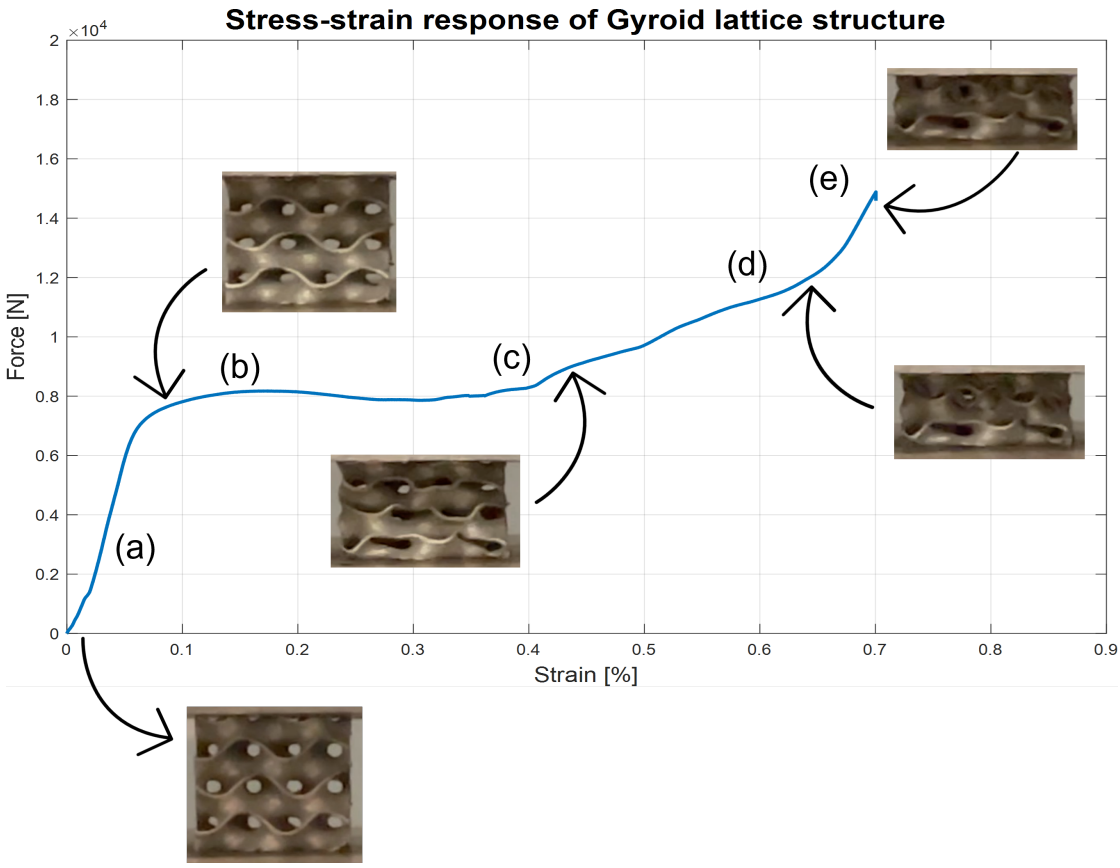

Figure 3.4: Compressive trend for structure Gyroid

3.6 Lattice images

In order to evaluate the quality of the manufacturing of the made samples, images have been produced for each cell type. The images obtained from the stereomicroscope showed more details on the visual quality of manufacturing. Figure 3.5 shows some digital microscope images of the lattice structures. The complete set of images are reported in Appendix. Looking at the pictures it is possible to state that all cells and struts of the lattice structure have been made with proper accuracy. No manufacturing and geometries errors of the lattice structure were detected. It

is possible to see a little bit of powder that has solidified around some of the more internal and complex shapes. Obviously without changing the shape and size of the cells. Therefore, it can be said that the geometry manufactured respects the CAD geometry with good accuracy.

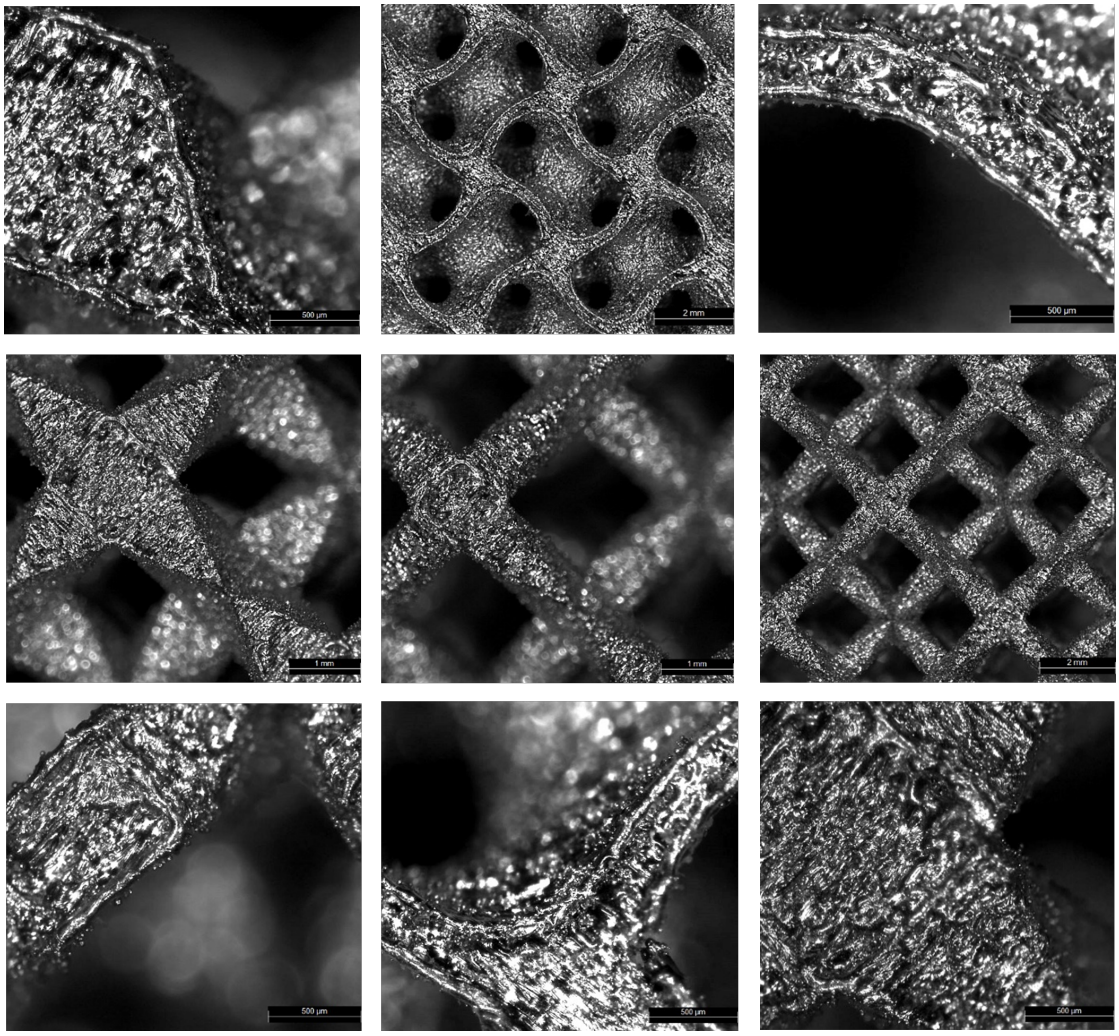

Figure 3.5: Stereomicroscopic images of some part of the lattice structures fabricated

4 Results and discussions

4.1 Compression test

For each cell and size, 3 specimens were tested and the curves were found to be quite similar. A mean curve was selected to represent a possible typical trend for that cell of that size. This procedure was carried out for each type and the graphs obtained are shown in Figure 4.1. As can be seen, on average smaller cells have higher load values. The slope of the elastic part is almost similar and all the structures do not show a specific collapse region.

To evaluate the stress vs strain curves, Equations 4.1 and 4.2 have been used:

$$\sigma = \frac{F}{A_0} \tag{4.1}$$

$$\epsilon = \frac{\delta}{l_0} \tag{4.2}$$

Where F is the load applied by the machine and δ is the displacement measured by the machine. Both these values represent the outputs of the test. A_0 and l_0 represent the area of the specimens and the initial length. The processed graphs are illustrated in Figure 4.2 where there is a division by cell type while in Figure 4.3 they have been divided according to the size of the unit cell. This division allows us to analyse from different points of view, firstly according to the type of cell and then according to the size of the cell and leaving aside its shape.

The first three graphs (Figure 4.1) show an average of the machine outcomes split by cell type and each curve represents the size of the base cell. It is possible to get an idea of the forces acting on the specimen. As it is possible to see the

three subsequent graphs show the relationship between stress and strain as shown by Equation 4.1 and Equation 4.2.

Comparing the various curves for each type, it can be seen that specimens with smaller cell sizes tend to have better mechanical responses. A curve that reaches much larger force values and also tends to have higher elastic moduli. As can be seen, there is an order of magnitude difference between Gyroid and Dode Medium lattice structure while the values of Dode Thick are still on average half those of the Gyroid ones.

The difference in behaviour between different unit cells is highly visible in the Gyroid structure where we know that there is a considerable difference between one structure and another in terms of the amount of material reacting to deformation. But it is also possible to see this phenomenon in Dode Medium and Dode Thick structures where the differences are very limited (1-2%). The curves show that the maximum stress value that the uniform lattice structures can support is at around 6%. While the densification region starts at around 35-45% of deformation. This means that the structures are able to maintain the load, and so to absorb energy for a long period of deformation.

When comparing the structures but with the same basic unit cell (Figure 4.3), it can be seen that the Gyroid structure has a better mechanical response in almost all configurations. The only difference is the unit cell 8 where (Figure 4.3 c) as it can be observed the Dode Thick structure reaches quite similar values of stresses. Obviously, these graphs do not take into account the relative density of each sample. To make a better comparison, the specific mechanical properties of the lattice structures (normalised to the relative density) were calculated. Figure 4.4 shows the normalised values. It can be seen that there are not many differences. The normalisation tends to slightly accentuate the difference between the Dode Thick/Dode Medium and Gyroid structures. From the graph (Figure 4.4 c), it is possible to note that even in the case of unit cell 8, contrary to what was seen before, the Gyroid topology has a higher specific stress curve. This aspect depends on the fact that graph of the Figure 4.3 (c) does not take into account the relative density of the structure.

Figure 4.1: Outcome of the compression test machine: Gyroid (a), Dode Medium (b), Dode Thick (c)

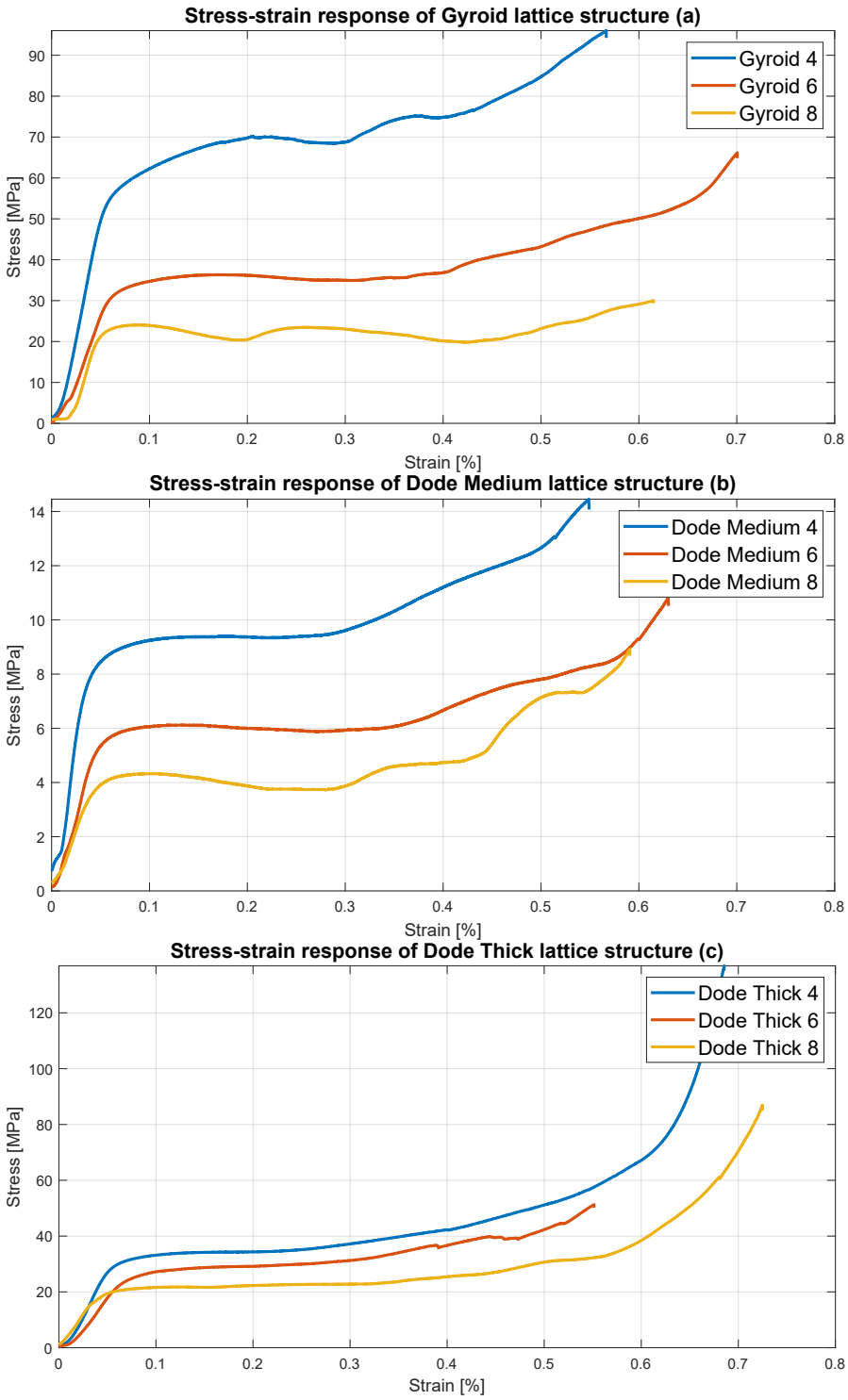

Figure 4.2: Stress vs Strain response splitted by lattice structures topology: Gyroid (a), Dode Medium (b), Dode Thick (c)

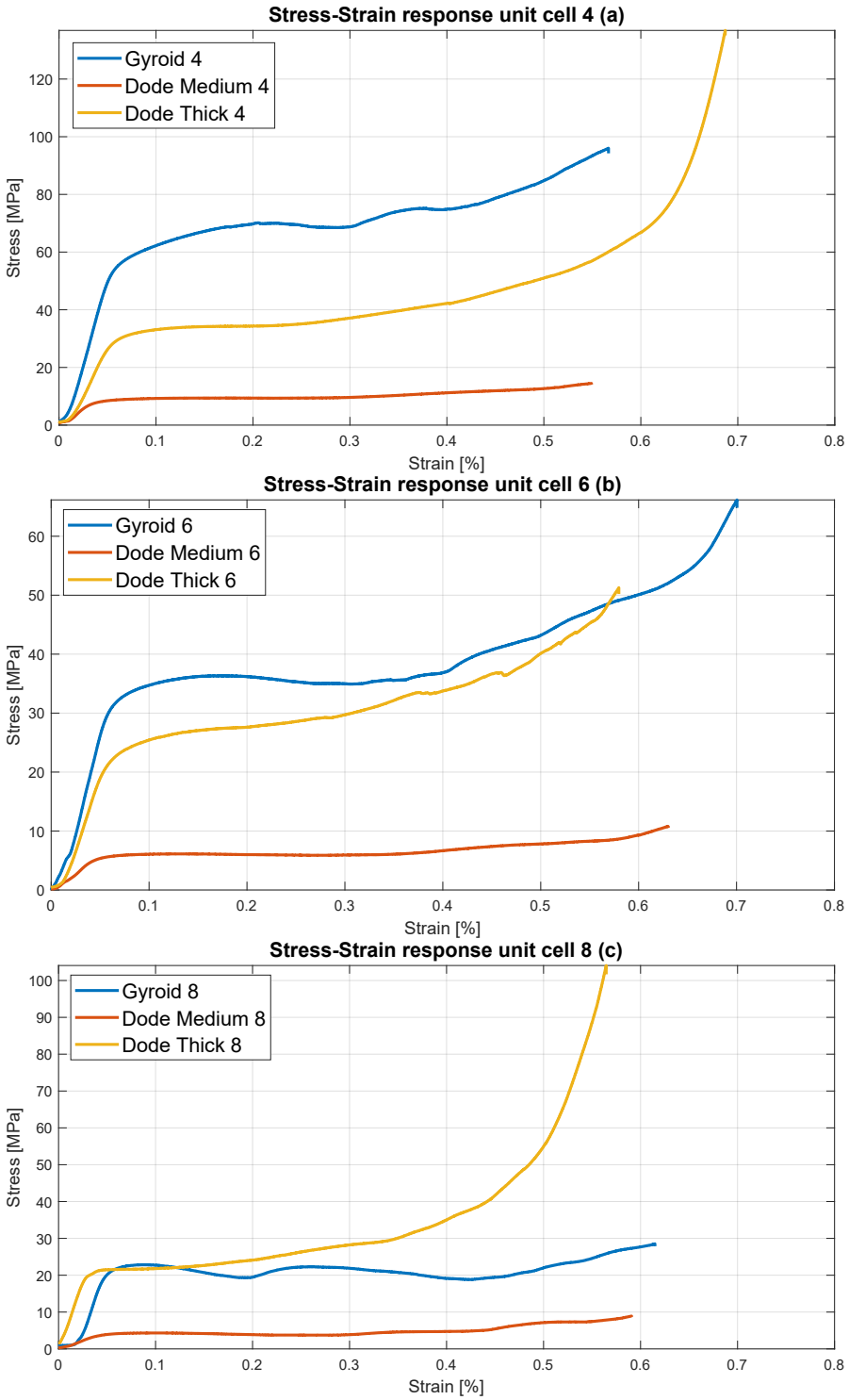

Figure 4.3: Stress vs Strain response splitted by unit cell dimension: Unit cell 4 (a) Unit cell 6 (b) Unit cell 8 (c)

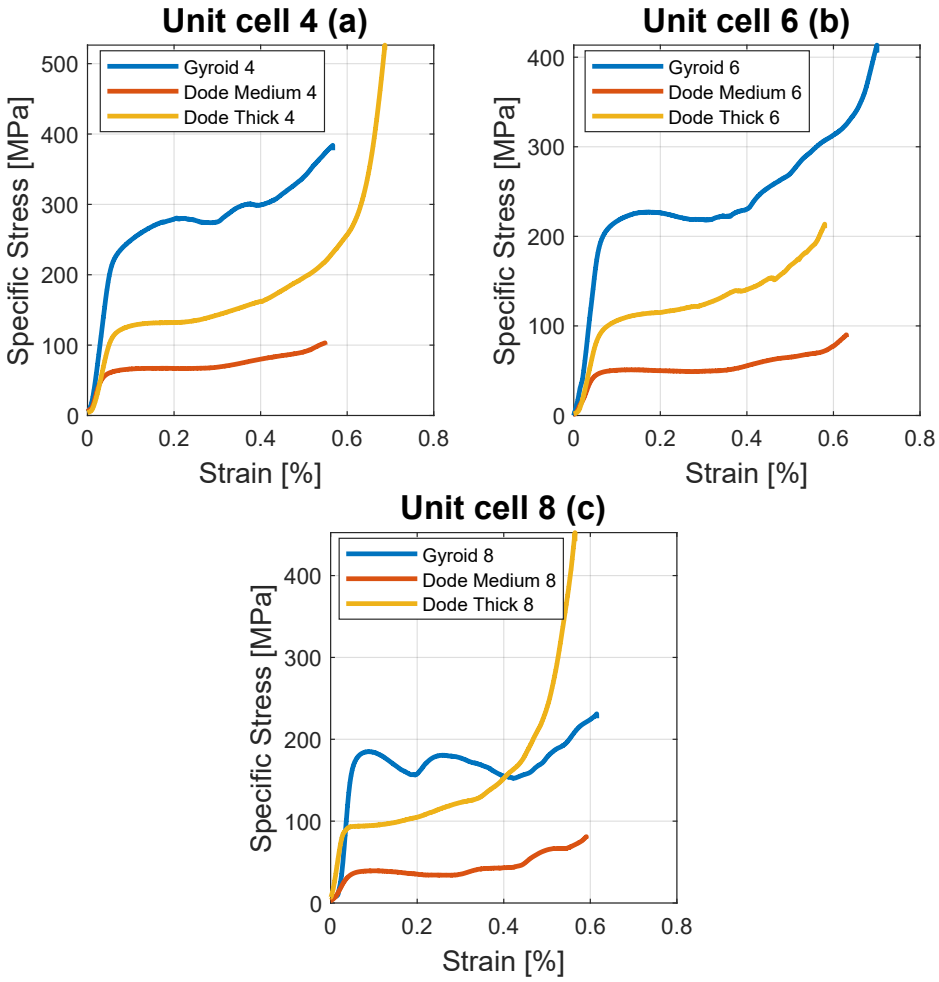

Figure 4.4: Specific stress vs Strain response of the lattice structure splitted by unit cell dimension: Unit cell 4 (a) Unit cell 6 (b) Unit cell 8 (c)

Normalizing all the parameters with respect to the density, we note that the situation is reversed because the Dode structure has a density that is almost twice that of the Gyroid structure. Considering this aspect as well, we can state with greater accuracy that the Gyroid typology, for all the basic cell dimensions analysed, presents trends and therefore better mechanical properties than the other two structures.

All the different parameters mentioned above were derived from the graphs shown above. The following formula was used to calculate Young's modulus values

(the slope of the elastic section):

$$E = \frac{\sigma_2 - \sigma_1}{\epsilon_2 - \epsilon_1} \tag{4.3}$$

Where the values of σ and ϵ were derived from the elastic and linear parts of the stress-strain characteristic curves. On the other hand, the UCS value was read directly from the graph. Table 4.1 lists the average values of the mentioned properties for each type of structure and size.

	Cell size $[mm]$	**Young modulus** $[MPa]$	**UCS** $[MPa]$
Gyroid	4	1145.30	67.98
	6	767.99	35.57
	8	1607.43	23.79
Dode Medium	4	218.35	9.54
	6	145.74	6.17
	8	105.08	4.24
Dode Thick	4	751.30	33.50
	6	485.49	28.21
	8	505.98	22.15

Table 4.1: Young's modulus and UCS calculated values

4.2 Young's Modulus

Based on the data present in Table 4.1, it was possible to generate the graph shown in Figure 4.5. Analysing the trends from Figure 4.5, it is possible to state that the values of the modulus of elasticity increase as the relative density increases. This growth trend is common to all structures. This allows us to better understand the behaviour of such a structure and to predict the value of the elastic modulus by

varying the relative density. From the values, we can also say that the values of the Gyroid structure are higher than those of the Dode structures in each configuration. It is also possible to state that the difference between Dode Medium and Gyroid remains more or less constant as the relative density changes. On the other hand, the difference between Dode Thick and Gyroid tends to decrease as the relative density increases. In order to make a more accurate comparison, it is necessary even in this case to normalise the values with respect to the relative density. In this way, Figure 4.6 can be obtained. It shows in a graph (a) the values divided into a bar graph for each unit cell size. In bar graph (b) the same values but normalised. Looking at the graph of the specific Young modulus, we can see that the differences between one dimension and the another are very attenuated. We can say that the trend is almost constant, especially for the Gyroid typology. This aspect proves that the differences obtained in the various unit cell size configurations depend mainly on the relative density factor. These values depend to a much lesser extent on a change in the size of the base cell.

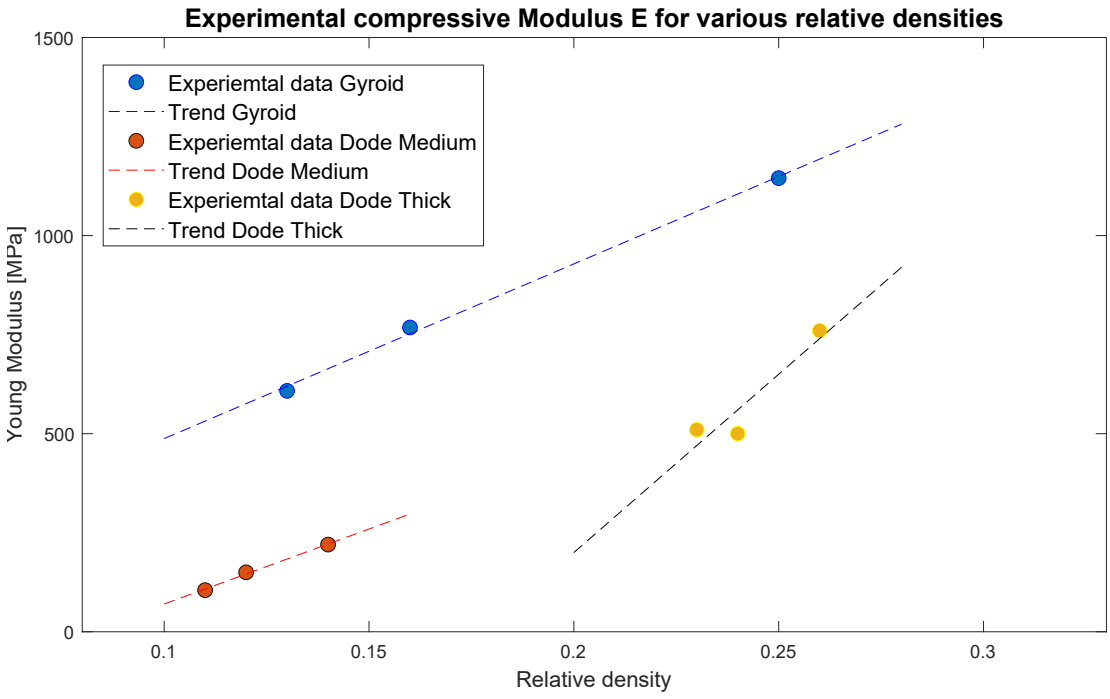

Figure 4.5: Experimental data and trends of the compressive modulus for each lattice structures

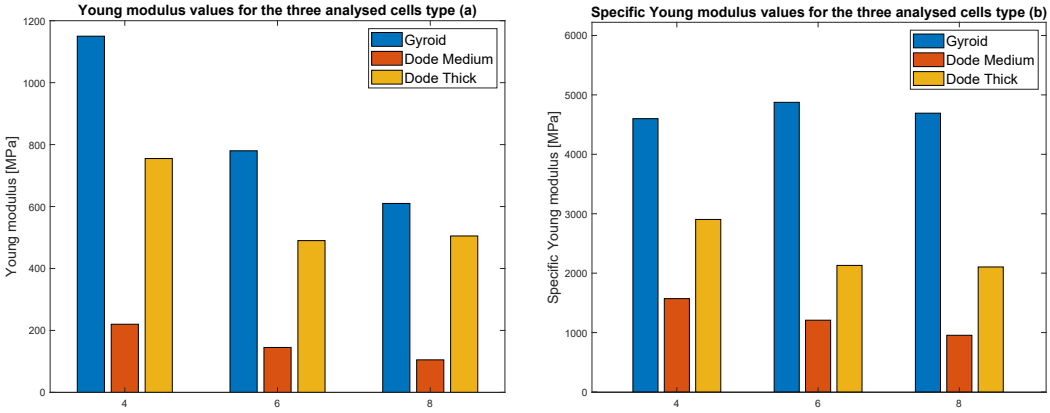

Figure 4.6: (a) Values of the compressive modulus (b) Values of the specific compressive modulus

4.3 Ultimate Compressive Strenght

Also in this case it was possible to generate the graph in Figure 4.7 from the data in Table 4.1. It is possible to observe from the graph that the trend is increasing as the relative density increases. As far as the UCS value is concerned, we can state that contrary to Young's modulus, in this case, the difference between the Gyroid structure and the others tends to increase as the relative density of the lattice structure increases. Also in this case it is possible to observe the variation of the UCS for each cell typology as shown in Figure 4.8 (a). The high value obtained for the Dode Thick 8 cell compared to the Gyroid 8 can also in this case be explained by the substantial difference in the material reacting to the load, in the value of its relative density. If we try, in fact, to plot the value of Specific UCS (Figure 4.8 b) we can observe how this difference is inverted. This data is very important to avoid drawing hasty and wrong conclusions from reading the data. As far as UCS is concerned, it is also possible to say that the Gyroid shows values that are almost double those of the Dode Thick structure and much larger than those of the Dode Medium.

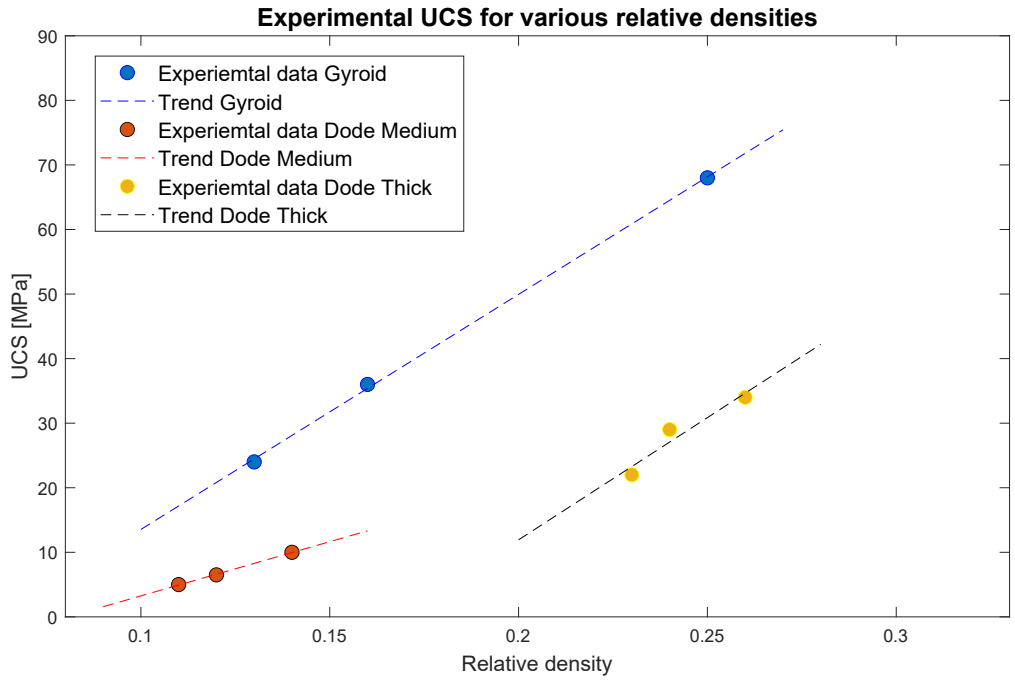

Figure 4.7: Experimental data and trends of UCS for each lattice structures

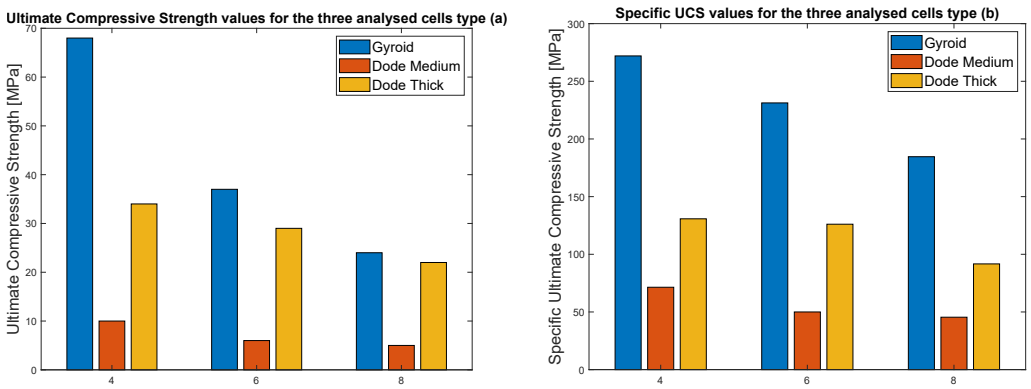

Figure 4.8: (a) Values of the UCS (b) Values of the specific UCS

4.4 SEA

The specific energy absorption (SEA) is one of the most important characteristics to evaluate the energy absorption capacity of the cellular material. It is defined as:

$$SEA = \frac{EA}{M} = \frac{\int_0^\delta F\, d\delta}{M} \tag{4.4}$$

where M is the mass of the structure, F is the compressive force, AE is the total energy absorbed by the cellular material, which can be calculated by the area under the load-displacement curves. In general, a higher SEA means a better energy absorption efficiency of the cellular material. The formula can be written also in the form:

$$SEA = \frac{\int_0^{\delta} F\, d\delta}{M} = \frac{\int_0^{\epsilon} \sigma(\epsilon)\, d\epsilon}{\rho^*} \tag{4.5}$$

In this way, we can link it to the density of the lattice structures. The integral at the numerator also represents the area under the curve of the stress vs strain graph. In this case, the SEA is evaluated considering up to a maximum of 60% strain; just before the beginning of the densification area.

In Table 4.2 all the values calculated are reported for all the cellular structures. While Figure 4.9 (a) shows the trends of the values according to the relative density parameter, in Figure 4.9 (b) the same values are shown divided by type and size of the unit cell. As expected, the Gyroid structure has the best values for energy absorption. This result is due to the high values of Young's modulus and UCS for this structure.

	Cell size	$\int_0^{\epsilon} F\, d\delta$	ρ^* $[g/mm^3]$	SEA $[J/g]$
Gyroid	4	42.14	0.001970	21.39
	6	21.57	0.001286	16.77
	8	13.08	0.001004	13.02
Dode Medium	4	6.35	0.001121	5.66
	6	3.83	0.000942	4.07
	8	2.92	0.000901	3.24
Dode Thick	4	24.58	0.002029	12.11
	6	21.12	0.001891	11.16
	8	19.61	0.001863	10.53

Table 4.2: SEA calculated values

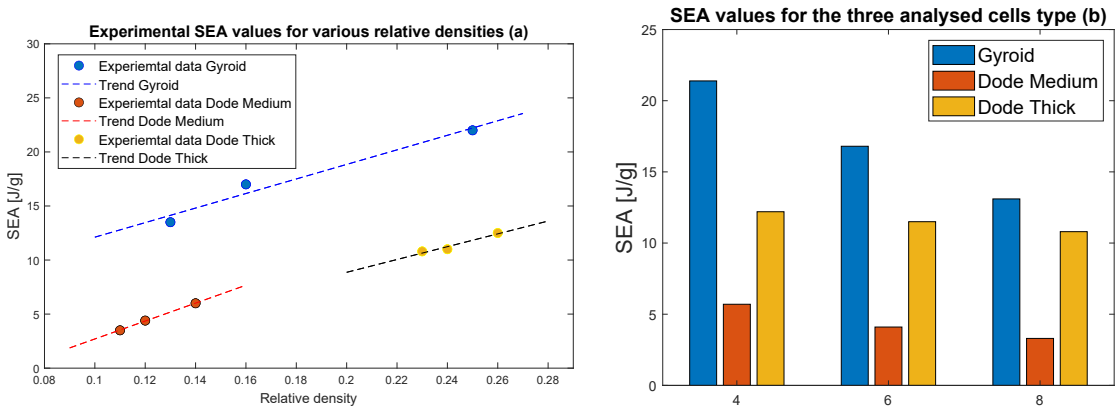

Figure 4.9: (a) Experimental data and trends of SEA for each lattice structures (b) SEA values

4.5 Comparison between experimental data and predictions of the Gibson-Ashby model

As illustrated in the previous chapter, the Gibson-Ashby model relates the relative density $\left(\frac{\rho^*}{\rho_s}\right)$ with the relative modulus $\left(\frac{E^*}{E_s}\right)$ or strength $\left(\frac{\sigma^*}{\sigma_s}\right)$ of a lattice structure material [7]. Again, it was possible to produce a graph that put all these parameters together. The graph in Figure 4.10 was then produced, which relates the relative density to the ratio of the elastic moduli. In Figure 4.11 instead, we can observe the relation between the relative density and the ratio between the Ultimate compressive strength. As stated in the previous chapter it is possible to highlight a certain range within which, according to the literature, lattice structures with bending-dominated behaviour operate. These ranges are highlighted in the graph and have been realised following the Equation:

Min	**Max**
$\frac{E^*}{E_s} = 4.0\left(\frac{\rho^*}{\rho_s}\right)^2$	$\frac{E^*}{E_s} = 0.1\left(\frac{\rho^*}{\rho_s}\right)^2$
$\frac{\sigma^*}{\sigma_s} = 1.0\ \left(\frac{\rho^*}{\rho_s}\right)^{3/2}$	$\frac{\sigma^*}{\sigma_s} = 0.1\ \left(\frac{\rho^*}{\rho_s}\right)^{3/2}$

From this comparison the following information is observed:

- As far as the modulus is concerned, not all values were found to fall within the predicted range.

- Values outside the expected range are those relating to the Dode structure. This range was generated based on the behaviour of open-celled metal foams and it is not unexpected that non-stochastic lattice structures with repeated unit cells may exhibit different behaviour. [38]

- Since the difference with the minimum line is not large, any underestimation of the modulus values could be the result of a not perfect execution of the compression test. This could be due to an imperfect alignment of the lattice structure with respect to the load cell and therefore to an imperfect application of the load perpendicular to the specimen.

- Another reason for these results could be related to an overestimation of the effective cross-section area reacting to the load from which the sigma value is derived. In fact, if an effective area is taken into account, we can see that its value is much smaller and therefore we will obtain slightly higher values which would place the points perfectly in the centre of the indicated range.

- As far as the Relative Ultimate Compression Strength values are concerned, we can see that they fall perfectly within the range.

- It can be appreciated that different structures occupy different positions within the range. This shows that the topological choice of structure affects the mechanical properties much more than the relative density value.

- UCS values are comparable to those obtained in the scientific literature

- In accordance with the literature, TPMS structures show higher values for both relative modulus and relative UCS.

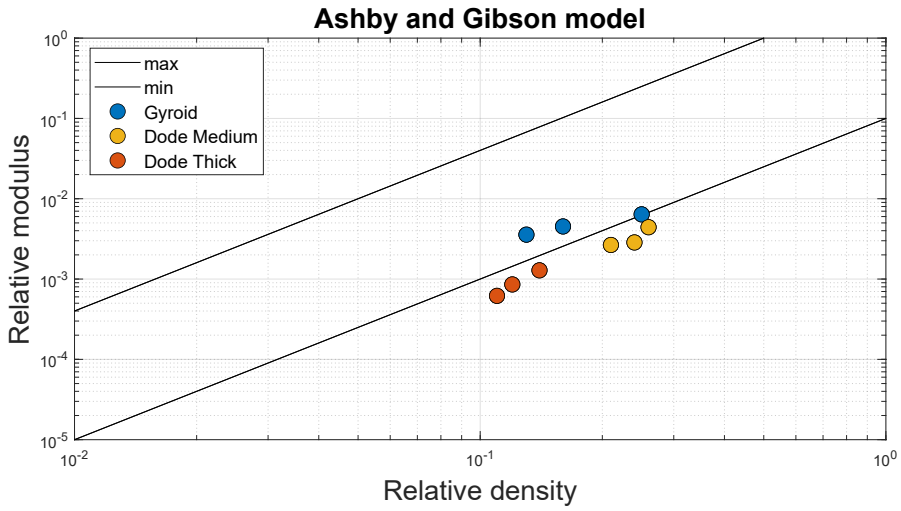

Figure 4.10: Comparison of reported experimental modulus data with prediction of the Gibson-Ashby model

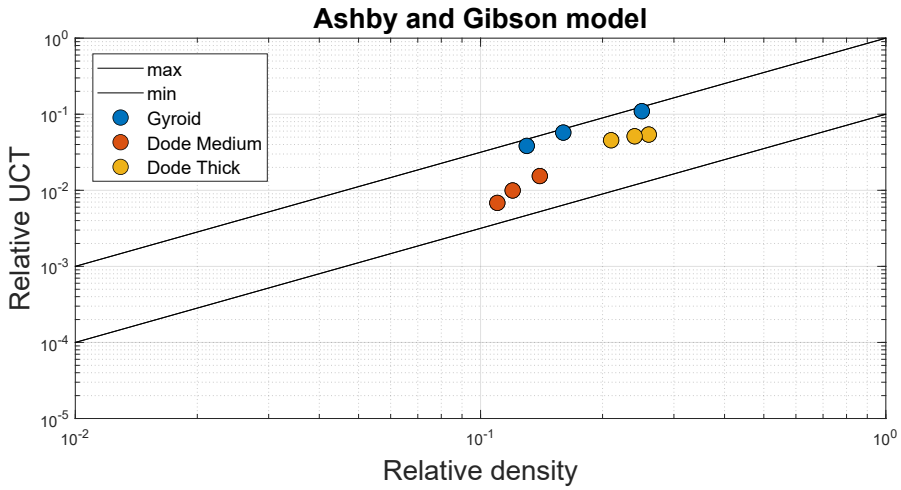

Figure 4.11: Comparison of reported experimental compressive strength data with prediction of the Gibson-Ashby model

4.6 Deformation modes

The collapse and deformation mechanism of the lattice structure in quasi-static compression loading is shown in Figure 4.12. The images are taken during testing at different strain levels. The first line represents the evolution of a Gyroid specimen, the second a Dode Thick, the third a Dode Medium structure. It is

worth mentioning here that the relative density at which these images are taken varies from one cell topology to another, however, for the same cell topology, the observed deformation pattern was the same for all relative densities considered. Thus, this deformation mechanism is not dependent on relative density and is highly dependent on cell topology. As shown in Figure 4.12 after a gradual collapse of the lattice structures, their struts were contacted, eventually creating a densification region, as it is possible to notice in the bottom part of the structure especially for the Dode Medium one. For the Gyroid structure where there are no struts inside the structure, we can see the surfaces of the various walls that come into contact. This is much more evident as the curved surfaces become horizontal, as shown in the first line of Figure 4.12. From the figure is possible to notice that the images show no signs of local brittleness failure. It is possible to state that lattice structures deformation is stable and smooth during the entire compression loading process.

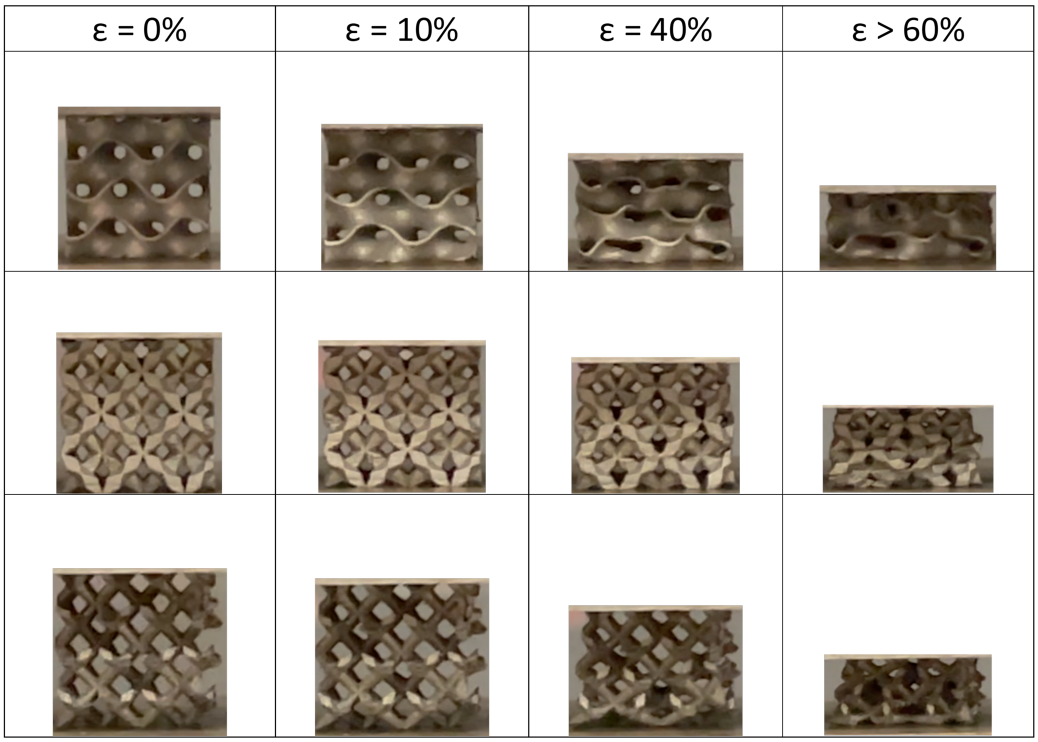

Figure 4.12: Lattice structures deformation and collapse mechanism in quasi-static compression testing

4.7 Simulation Analysis

As stated in section 2.7 , another important tool for predicting the behaviour of lattice structures is simulation. In this case, homogenisation was used in order to compare the behaviour in terms of mechanical properties (i.e. stiffness) of the different unit cells. This technique allows us to obtain the stiffness matrix for a given geometry. The matrix can then be exported and treated as a material for other simulations. To perform this kind of analysis, the software nTopology has been used. Within this software, there is a specific tool that carries out the whole simulation. Starting from an implicit body, a surface mesh was generated and subsequently redefined to obtain a very accurate tetrahedral solid mesh. At this point, the characteristics of the material composing the structure were assigned, specifically E and ν of material 316L. The homogenization tool automatically sets up the boundary conditions and loads. The six fundamentals loads (3 axial, 3 shears) are applied. As output, it is possible to get the deformation in a specific direction (applying each of the 6 fundamental loads) but also a polar plot representing the directional stiffness. The directional stiffness gives us an idea of how the material behaves in different directions. The magnitude is referred to Young's modulus, so it allows us to visually see which directions our structure reacts best to directional loads. At the same time, it allows us to note any symmetries or dissymmetries. This is an important factor, especially for cells (e.g. honeycomb), which present a strong dissymmetry (one direction presents a much greater stiffness than the other), allowing us to understand how to use that type of lattice and above all to apply that structure when we know that the load applied are along the direction that presents greater stiffness. In the case of a load case with loads in different directions, a structure with a more symmetrical plot is preferable and would respond better to the stresses.

The following graphs (Figura 4.13, 4.14, 4.15) show (in order):

- The images of the solid mesh made
- The image of the deformation (magnitude) in the z-direction that represents the same direction as the compression tests carried out experimentally

- The directional stiffness as a polar plot with the magnitude of the Young modulus

The graphs show that the gyroid structure is very symmetrical without the presence of principal directions in which the stiffness is greater. This type of information is perfectly in line with expectations, the gyroid structure being very symmetrical. At the same time, the two Dode structures show a very similar configuration, which is to be expected. In particular, small, symmetrically distributed areas of increased stiffness can be seen. Even though the homogenization method is considered not suitable for a low number of unit cells, in our case of uniaxial load provided an accurate estimate of the linear behaviour of the lattice.

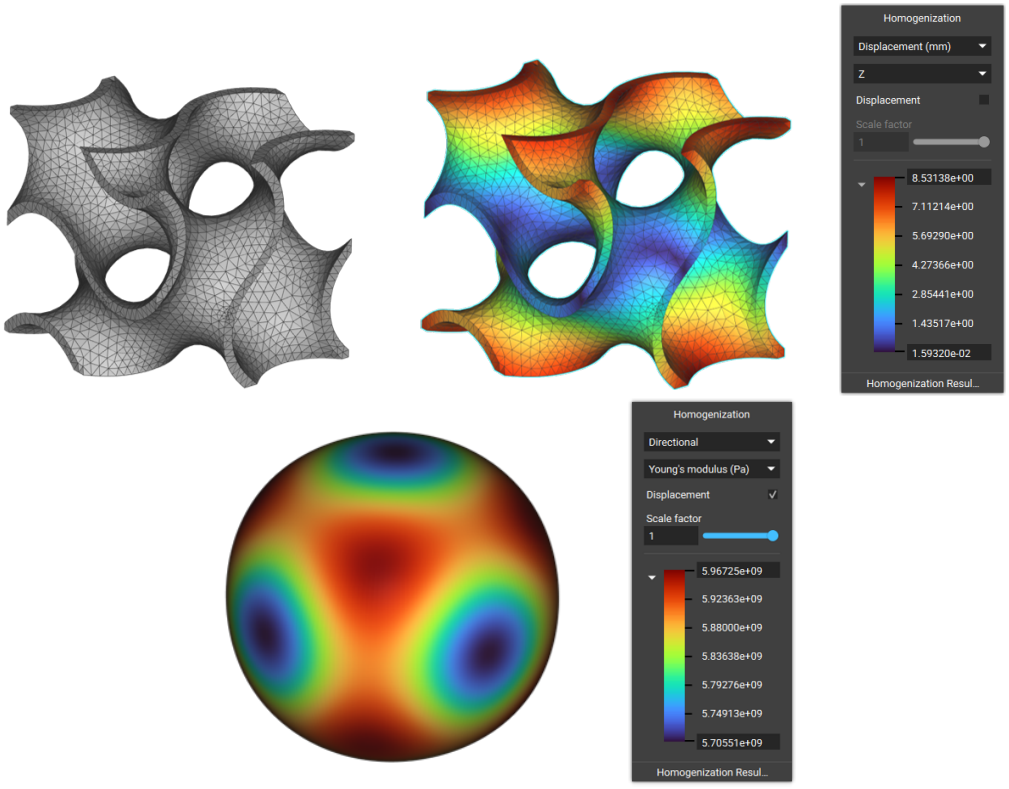

Figure 4.13: Gyroid: Solid mesh - Deformation magnitude (Z-direction) - Directional stiffness

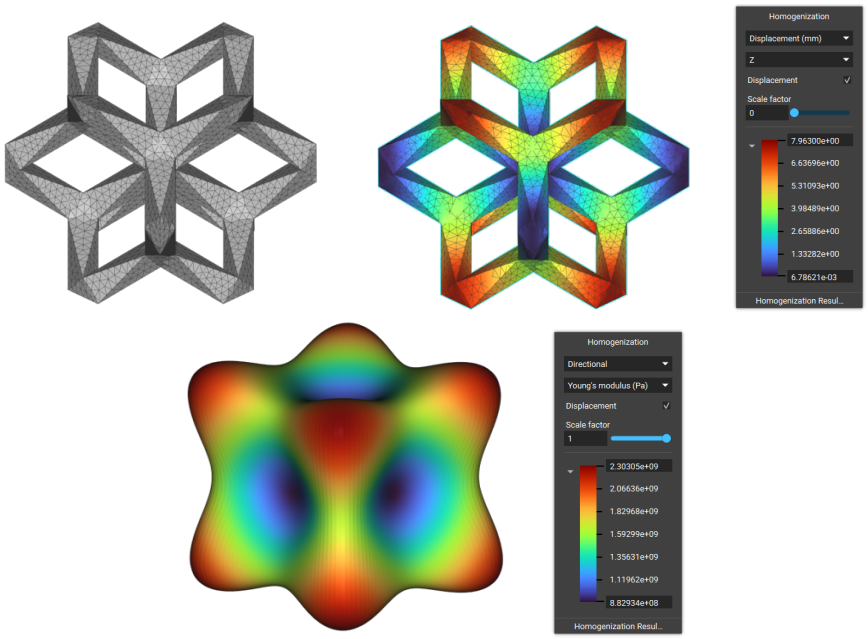

Figure 4.14: Dode Medium: Solid mesh - Deformation magnitude (Z-direction) - Directional stiffness

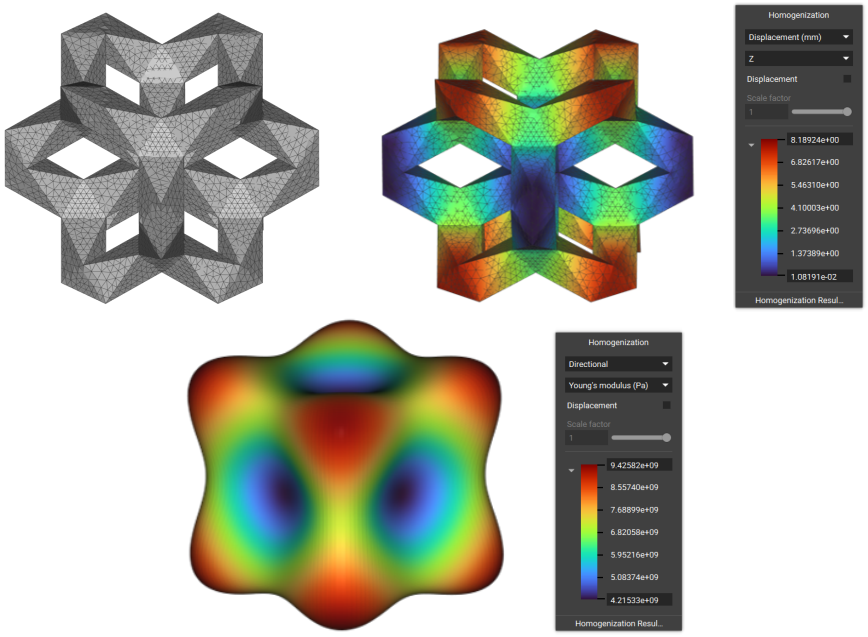

Figure 4.15: Dode Thick: Solid mesh - Deformation magnitude (Z-direction) - Directional stiffness

As mentioned above, another important piece of information that can be exported from the simulation tool is the stiffness matrix of each structure. This step was carried out for each type of unit cell and the values were imported into Matlab. From theory the following equations hold:

$$[S] = [C]^{-1} \tag{4.6}$$

$$\frac{1}{E_{xx}} = S_{xx,xx} \tag{4.7}$$

Where E_{xx} is Young's Modulus along the direction xx (and for symmetry reasons $E_{xx} = E_{yy} = E_{zz}$), $[C]$ is the stiffness matrix and $[S]$ is the so called compliance matrix. The compliance matrix has the following form:

$$\begin{bmatrix} \epsilon_{xx} \\ \epsilon_{yy} \\ \epsilon_{zz} \\ \epsilon_{yz} \\ \epsilon_{zx} \\ \epsilon_{xy} \end{bmatrix} = \begin{bmatrix} \frac{1}{E_{xx}} & -\frac{\nu_{yx}}{E_{yy}} & -\frac{\nu_{zx}}{E_{zz}} & 0 & 0 & 0 \\ -\frac{\nu_{yx}}{E_{xx}} & \frac{1}{E_{yy}} & -\frac{\nu_{zy}}{E_{zz}} & 0 & 0 & 0 \\ -\frac{\nu_{xz}}{E_{xx}} & -\frac{\nu_{yz}}{E_{yy}} & \frac{1}{E_{yy}} & 0 & 0 & 0 \\ 0 & 0 & 0 & \frac{1}{2G_{yz}} & 0 & 0 \\ 0 & 0 & 0 & 0 & \frac{1}{2G_{zx}} & 0 \\ 0 & 0 & 0 & 0 & 0 & \frac{1}{2G_{xy}} \end{bmatrix} \begin{bmatrix} \sigma_{xx} \\ \sigma_{yy} \\ \sigma_{zz} \\ \sigma_{yz} \\ \sigma_{zx} \\ \sigma_{xy} \end{bmatrix} \tag{4.8}$$

From this matrix is possible to get the elastic modulus.

As it is possible to notice, the compliance matrix has lots of zeros entries. If we calculate this kind of matrix for our unit cells it is possible to get a visual display of the compliance matrix in order to observe qualitatively how much our matrix differs from the theoretical one.

This visual display allows us to understand to which extent our structures can be defined as orthotropic. The image of the Anisotropy of Compliance Matrix is shown in Figure 4.16.

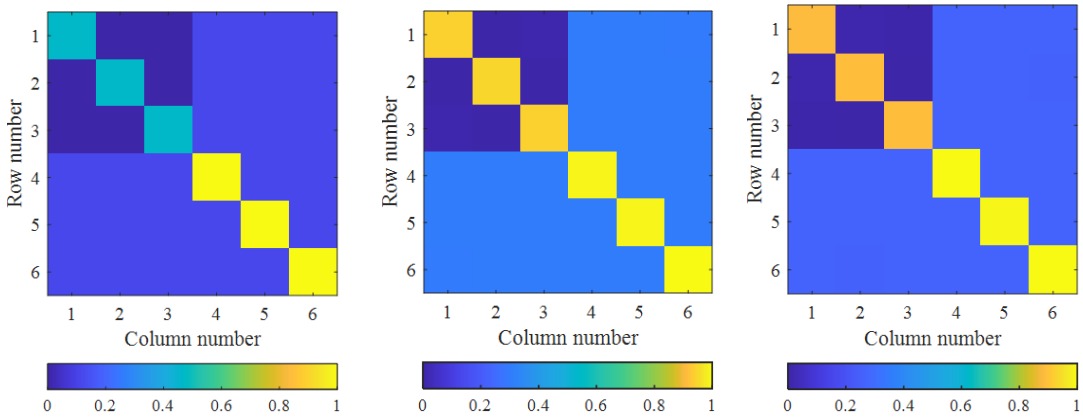

Figure 4.16: Visual display of compliance matrices: Gyroid - Dode Medium - Dode Thick

5 Conclusions

In this thesis work, the theory that studies the behaviour of lattice structures was analysed, attempting to investigate the various aspects and properties that have been studied and analysed in the literature. As for the experimental part, the objective was the characterisation of certain structures. Once the unitary cells had been identified, we moved on to the modelling of the specimens using Magics software. The specimens were then used to extrapolate and characterise the chosen structures. Compression tests were used to highlight the behaviour and extrapolate the elasticity and load values. From this first step, we can deduce that the stress-strain curves obtained are in line with the expected behaviour illustrated in theory. As far as the values obtained are concerned, they are also in accordance with the values found in the literature. The application of the Gibson-Ashby model allows us to observe that the values obtained fall within the expected range.

From a first analysis, it is possible to state that the Gyroid structure in all the analysed areas (Yong Modulus, UCS, SEA) has better characteristics than the Dode structures both in absolute values and in specific values. The results showed that the Young's Modulus of the Gyroid can be tuned in the range of $600 \div 1200$ MPa with a relative density in the range of 10-25%. It is also possible to observe that all the configurations show a clear long, flat plateau stress, this characteristic being fundamental for an optimal energy absorption behaviour. We can affirm that for the analysed structures the output values depend on the relative density but also and above all on the choice of the base cell. The different behaviour of the structure was in fact also confirmed by the numerical analysis carried out, which showed above all that the Gyroid structure has greater isotropy and a fairly evenly

distributed directional stiffness. However, the Dode structures also showed rather positive values. The Homogenization technique was useful to extract the ideal characteristics when the lattice is theoretically infinite and in this case, obtained good results.

Future studies of this work could develop a FEM analysis to obtain more accurate values and to monitor stress and strain values locally with greater precision. It could also be useful to better analyse the behaviour of the structure under load (deformation modes). Tests could also be carried out to analyse the crash behaviour and thus investigate the whole energy absorption part. The aim of this thesis was to characterise lattice structure specimens, but it would certainly be interesting to study the behaviour of a real part made with a lattice structure. In which loads and constraints of the structure are taken into account and optimised to obtain the best achievable characteristics.

6 Appendix

Here are reported the complete set of images for all the configurations type

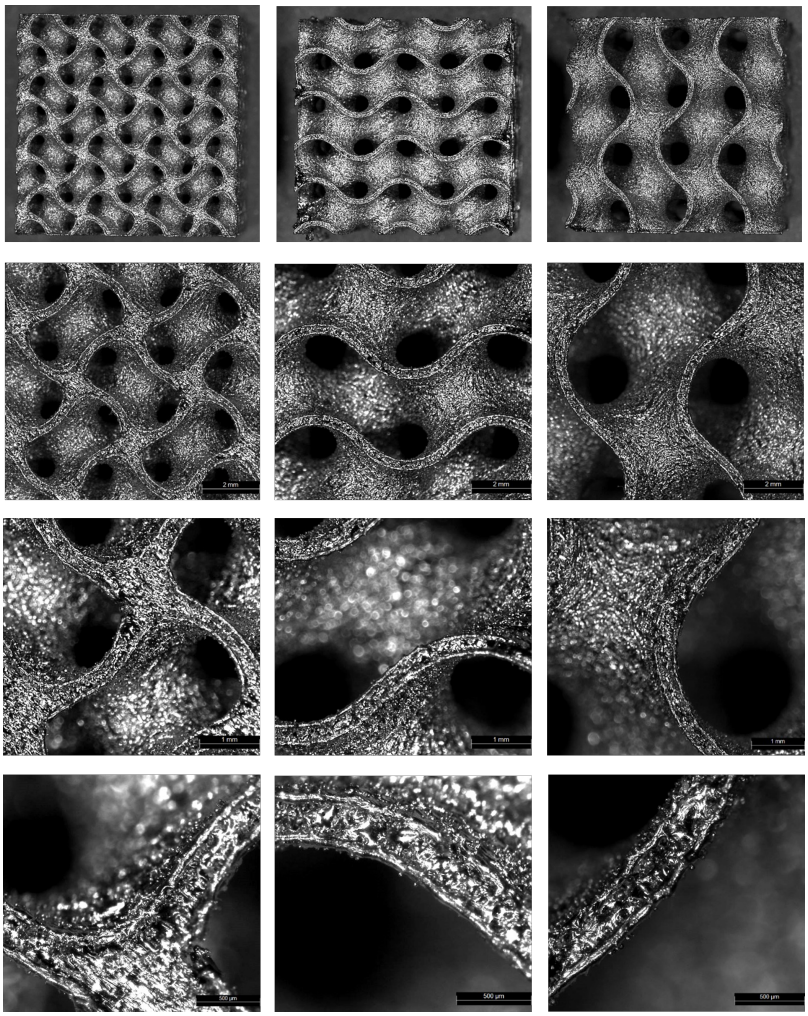

Figure 6.1: Gyroid: 4 - 6 - 8

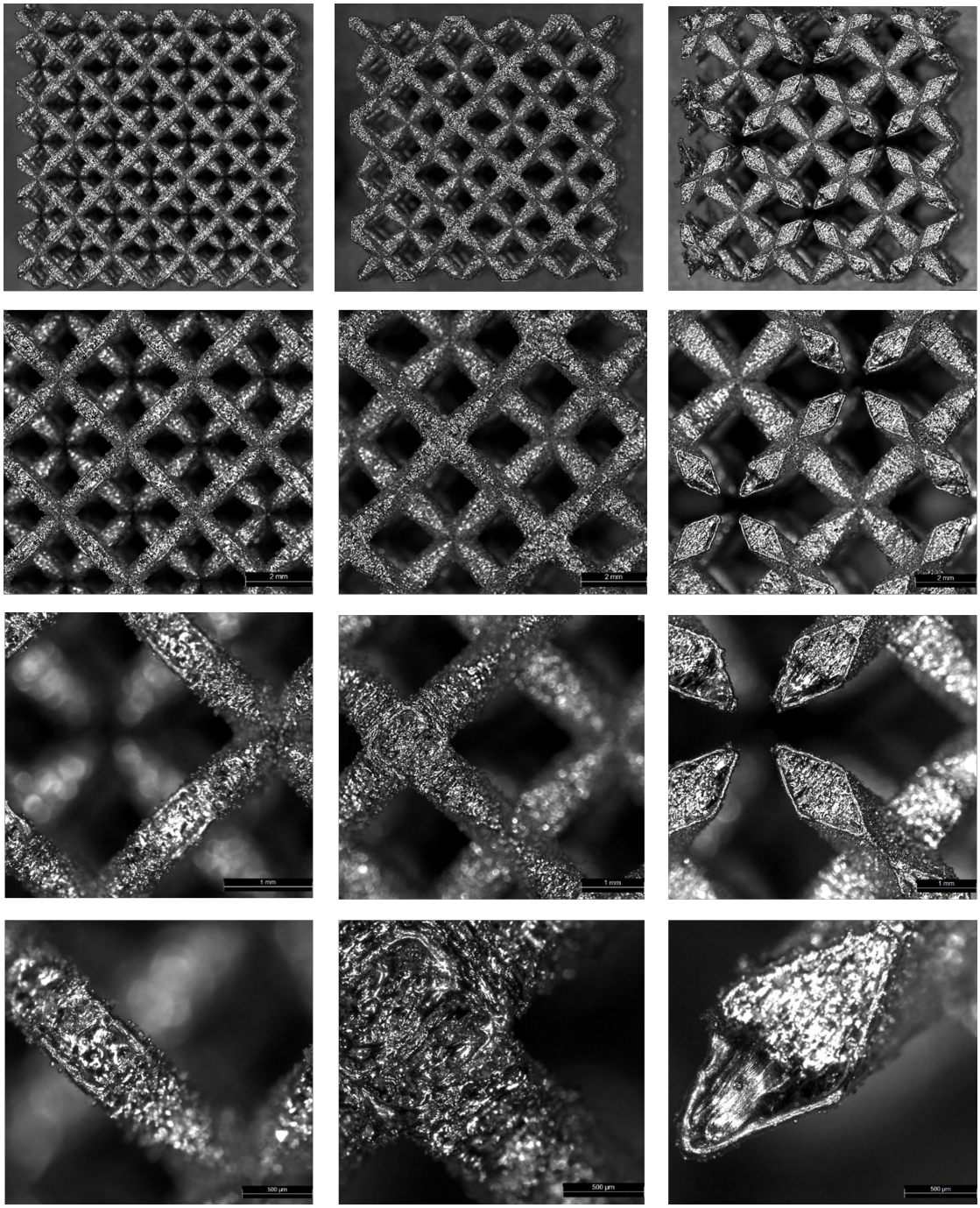

Figure 6.2: Dode Medium: 4 - 6 - 8

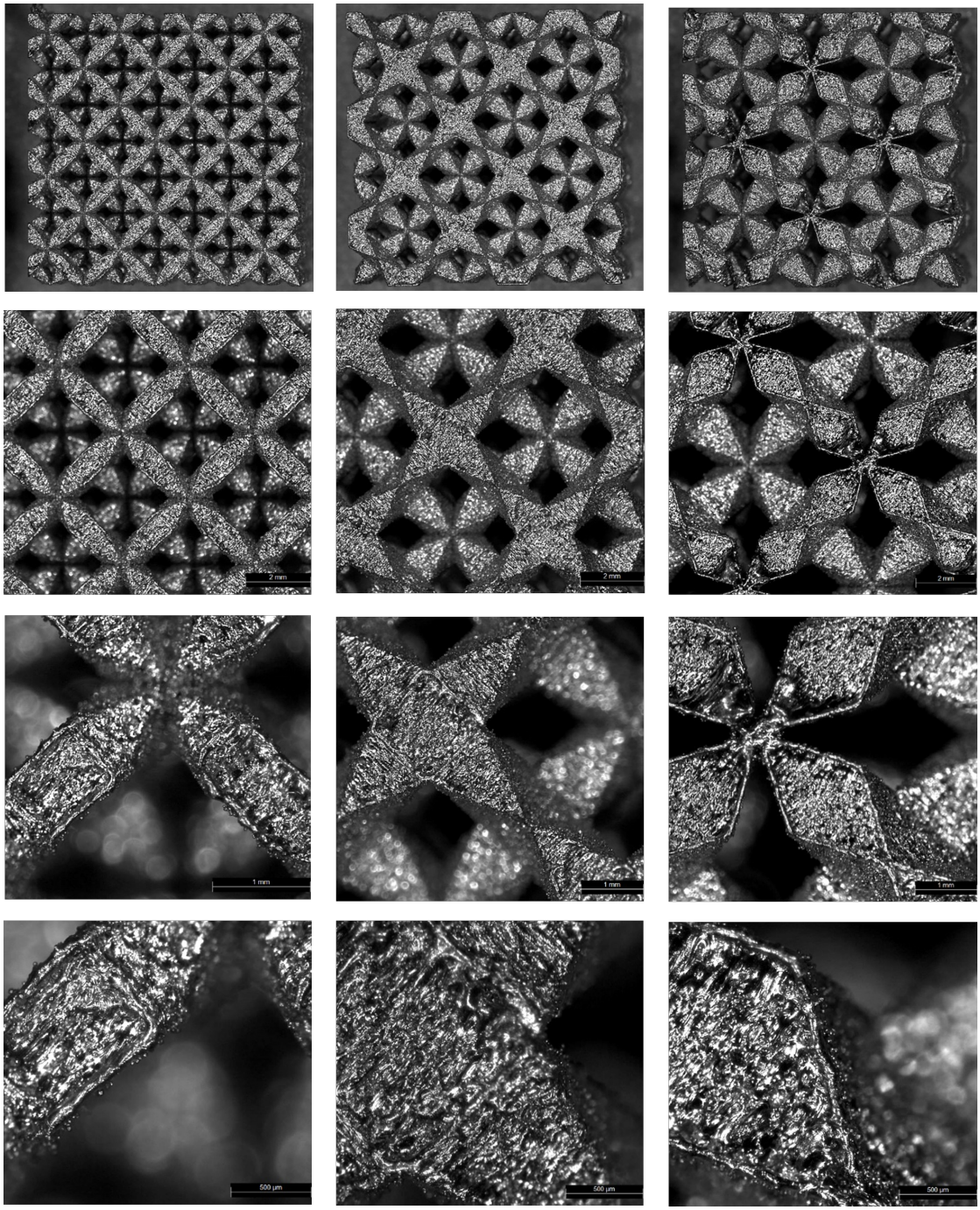

Figure 6.3: Dode Thick: 4 - 6 - 8

7 Bibliography

[1] ASTM F2792-12a, "Standard Terminology for Additive Manufacturing Technologies, (Withdrawn 2015)," doi: 10.1520/F2792-12A.

[2] Y. Ibrahim, C. M. Davies, C. Maharaj, Z. Li, J. P. Dear, and P. A. Hooper, "Post-yield performance of additive manufactured cellular lattice structures," Prog. Addit. Manuf., vol. 5, no. 2, pp. 211–220, 2020, doi: 10.1007/s40964-020-00128-4.

[3] F. Rosa, S. Manzoni, and R. Casati, "Damping behavior of 316L lattice structures produced by Selective Laser Melting," Mater. Des., vol. 160, pp. 1010–1018, 2018, doi: https://doi.org/10.1016/j.matdes.2018.10.035.

[4] S. Beretta and S. Romano, "A comparison of fatigue strength sensitivity to defects for materials manufactured by AM or traditional processes," Int. J. Fatigue, vol. 94, pp. 178–191, 2017, doi: https://doi.org/10.1016/j.ijfatigue.2016.06.020.

[5] D. L. Bourell, "Perspectives on Additive Manufacturing," Annu. Rev. Mater. Res., vol. 46, no. 1, pp. 1–18, 2016, doi: 10.1146/annurev-matsci-070115-031606.

[6] L. J. Gibson, "Modelling the mechanical behavior of cellular materials," Mater. Sci. Eng. A, vol. 110, pp. 1–36, 1989, doi: https://doi.org/10.1016/0921-5093(89)90154-8.

[7] L. J. Gibson and M. F. Ashby, Cellular Solids: Structure and Properties, 2nd ed. Cambridge University Press, 1997.

[8] D. Wang, Y. Yang, R. Liu, D. Xiao, and J. Sun, "Study on the designing rules and processability of porous structure based on selective laser melting (SLM)," J. Mater. Process. Technol., vol. 213, no. 10, pp. 1734–1742, 2013, doi: https://doi.org/10.1016/j.jmatprotec.2013.05.001.

[9] M. F. Ashby, "The properties of foams and lattices.," Philos. Trans. Ser. A, Math. Phys. Eng. Sci., vol. 364, no. 1838, pp. 15–30, Jan. 2006, doi: 10.1098/rsta.2005.1678.

[10] C. Pan, Y. Han, and J. Lu, "Design and Optimization of Lattice Structures: A Review," Appl. Sci., vol. 10, no. 18, 2020, doi: 10.3390/app10186374.

[11] G. Dong, Y. Tang, and Y. F. Zhao, "A Survey of Modeling of Lattice Structures Fabricated by Additive Manufacturing," J. Mech. Des., vol. 139, no. 10, 2017, doi: 10.1115/1.4037305.

[12] V. S. Deshpande, M. F. Ashby, and N. A. Fleck, "Foam topology: bending versus stretching dominated architectures," Acta Mater., vol. 49, no. 6, pp. 1035–1040, 2001, doi: https://doi.org/10.1016/S1359-6454(00)00379-7.

[13] J. C. M. F.R.S., "L. On the calculation of the equilibrium and stiffness of frames," London, Edinburgh, Dublin Philos. Mag. J. Sci., vol. 27, no. 182, pp. 294–299, 1864, doi: 10.1080/14786446408643668.

[14] Y. Shen, S. Mckown, S. Tsopanos, C. J. Sutcliffe, R. A. W. Mines, and W. J. Cantwell, "The Mechanical Properties of Sandwich Structures Based on Metal Lattice Architectures," J. Sandw. Struct. & Mater., vol. 12, no. 2, pp. 159–180, 2010, doi: 10.1177/1099636209104536.

[15] D. Kang, S. Park, Y. Son, S. Yeon, S. H. Kim, and I. Kim, "Multi-lattice inner structures for high-strength and light-weight in metal selective laser melting process," Mater. Des., vol. 175, p. 107786, 2019, doi: https://doi.org/10.1016/j.matdes.2019.107786.

[16] Milan Brandt, Laser Additive Manufacturing Materials, Design, Technologies, and Applications. 2017.

[17] T. Maconachie et al., "SLM lattice structures: Properties, performance, applications and challenges," Mater. Des., vol. 183, p. 108137, 2019, doi: https://doi.org/10.1016/j.matdes.2019.108137.

[18] Z. Xiao, Y. Yang, R. Xiao, Y. Bai, C. Song, and D. Wang, "Evaluation of topology-optimized lattice structures manufactured via selective laser melting," Mater. Des., vol. 143, pp. 27–37, 2018, doi: https://doi.org/10.1016/j.matdes.2018.01.023.

[19] H. Lei et al., "Evaluation of compressive properties of SLM-fabricated multi-layer lattice structures by experimental test and -CT-based finite element analysis," Mater. Des., vol. 169, p. 107685, 2019, doi: https://doi.org/10.1016/j.matdes.2019.107685.

[20] N. Novak et al., "Quasi-static and dynamic compressive behaviour of sheet TPMS cellular structures," Compos. Struct., vol. 266, p. 113801, 2021, doi: https://doi.org/10.1016/j.compstruct.2021.113801.

[21] D. Ashouri et al., "Mechanical behaviour of additive manufactured 316L f2ccz lattice structure under static and cyclic loading," Int. J. Fatigue, vol. 134, p. 105503, 2020, doi: https://doi.org/10.1016/j.ijfatigue.2020.105503.

[22] P. Płatek, J. Sienkiewicz, J. Janiszewski, and F. Jiang, "Investigations on Mechanical Properties of Lattice Structures with Different Values of Relative Density Made from 316L by Selective Laser Melting (SLM)," Materials (Basel)., vol. 13, no. 9, 2020, doi: 10.3390/ma13092204.

[23] K. Ushijima, W. J. Cantwell, R. A. W. Mines, S. Tsopanos, and M. Smith, "An investigation into the compressive properties of stainless steel micro-lattice structures," J. Sandw. Struct. & Mater., vol. 13, no. 3, pp. 303–329, 2011, doi: 10.1177/1099636210380997.

[24] M. M. Osman, M. Shazly, E. A. El-Danaf, P. Jamshidi, and M. M. Attallah, "Compressive behavior of stretched and composite microlattice metamaterial for energy absorption applications," Compos. Part B Eng., vol. 184, p. 107715, 2020, doi: https://doi.org/10.1016/j.compositesb.2019.107715.

[25] X. Cao et al., "Dynamic compressive behavior of a modified additively manufactured rhombic dodecahedron 316L stainless steel lattice structure," Thin-Walled Struct., vol. 148, p. 106586, 2020, doi: https://doi.org/10.1016/j.tws.2019.106586.

[26] M. Helou and S. Kara, "Design, analysis and manufacturing of lattice structures: an overview," Int. J. Comput. Integr. Manuf., vol. 31, no. 3, pp. 243–261, 2018, doi: 10.1080/0951192X.2017.1407456.

[27] D.-W. Lee, K. A. Khan, and R. K. Abu Al-Rub, "Stiffness and yield strength of architectured foams based on the Schwarz Primitive triply periodic minimal surface," Int. J. Plast., vol. 95, pp. 1–20, 2017, doi: https://doi.org/10.1016/j.ijplas.2017.03.005.

[28] E. Alabort, D. Barba, and R. C. Reed, "Design of metallic bone by additive manufacturing," Scr. Mater., vol. 164, pp. 110–114, 2019, doi: https://doi.org/10.1016/j.scriptamat.2019.01.022.

[29] Y. Xu, T. Li, X. Cao, Y. Tan, and P. Luo, "Compressive Properties of 316L Stainless Steel Topology-Optimized Lattice Structures Fabricated by Selective Laser Melting," Adv. Eng. Mater., vol. 23, no. 3, p. 2000957, 2021, doi: https://doi.org/10.1002/adem.202000957.

[30] G. Wang et al., "Design and Compressive Behavior of Controllable Irregular Porous Scaffolds: Based on Voronoi-Tessellation and for Additive Manufacturing," ACS Biomater. Sci. Eng., vol. 4, no. 2, pp. 719–727, Feb. 2018, doi: 10.1021/acsbiomaterials.7b00916.

[31] S. Tsopanos et al., "The Influence of Processing Parameters on the Mechanical Properties of Selectively Laser Melted Stainless Steel Microlattice Structures," J. Manuf. Sci. Eng., vol. 132, no. 4, 2010, doi: 10.1115/1.4001743.

[32] L. Zhang et al., "Energy absorption characteristics of metallic triply periodic minimal surface sheet structures under compressive loading," Addit. Manuf., vol. 23, pp. 505–515, 2018, doi: https://doi.org/10.1016/j.addma.2018.08.007.

[33] R. Gümrük and R. A. W. Mines, "Compressive behaviour of stainless steel micro-lattice structures," Int. J. Mech. Sci., vol. 68, pp. 125–139, 2013, doi: https://doi.org/10.1016/j.ijmecsci.2013.01.006.

[34] S. McKown et al., "The quasi-static and blast loading response of lattice structures," Int. J. Impact Eng., vol. 35, no. 8, pp. 795–810, 2008, doi: https://doi.org/10.1016/j.ijimpeng.2007.10.005.

[35] M. Smith, Z. Guan, and W. J. Cantwell, "Finite element modelling of the compressive response of lattice structures manufactured using the selective laser melting technique," Int. J. Mech. Sci., vol. 67, pp. 28–41, 2013, doi: https://doi.org/10.1016/j.ijmecsci.2012.12.004.

[36] C. Yan, L. Hao, A. Hussein, and D. Raymont, "Evaluations of cellular lattice structures manufactured using selective laser melting," Int. J. Mach. Tools Manuf., vol. 62, pp. 32–38, 2012, doi: https://doi.org/10.1016/j.ijmachtools.2012.06.002.

[37] C. Yan, L. Hao, A. Hussein, P. Young, and D. Raymont, "Advanced lightweight 316L stainless steel cellular lattice structures fabricated via selective laser melting," Mater. Des., vol. 55, pp. 533–541, 2014, doi: https://doi.org/10.1016/j.matdes.2013.10.027.

[38] T. Tancogne-Dejean, A. B. Spierings, and D. Mohr, "Additively-manufactured metallic micro-lattice materials for high specific energy absorption under static and dynamic loading," Acta Mater., vol. 116, pp. 14–28, 2016, doi: https://doi.org/10.1016/j.actamat.2016.05.054.

[39] H. Guo, A. Takezawa, M. Honda, C. Kawamura, and M. Kitamura, "Finite element simulation of the compressive response of additively manufactured lattice structures with large diameters," Comput. Mater. Sci., vol. 175, p. 109610, 2020, doi: https://doi.org/10.1016/j.commatsci.2020.109610.

[40] D. Li, W. Liao, N. Dai, and Y. M. Xie, "Comparison of Mechanical Properties and Energy Absorption of Sheet-Based and Strut-Based Gyroid Cellular

Structures with Graded Densities," Materials (Basel)., vol. 12, no. 13, 2019, doi: 10.3390/ma12132183.

[41] S. Ma, Q. Tang, Q. Feng, J. Song, X. Han, and F. Guo, "Mechanical behaviours and mass transport properties of bone-mimicking scaffolds consisted of gyroid structures manufactured using selective laser melting," J. Mech. Behav. Biomed. Mater., vol. 93, pp. 158–169, 2019, doi: https://doi.org/10.1016/j.jmbbm.2019.01.023.

[42] A. Zargarian, M. Esfahanian, J. Kadkhodapour, S. Ziaei-Rad, and D. Zamani, "On the fatigue behavior of additive manufactured lattice structures," Theor. Appl. Fract. Mech., vol. 100, pp. 225–232, 2019, doi: https://doi.org/10.1016/j.tafmec.2019.01.012.

[43] D. W. Abueidda, R. K. Abu Al-Rub, A. S. Dalaq, D.-W. Lee, K. A. Khan, and I. Jasiuk, "Effective conductivities and elastic moduli of novel foams with triply periodic minimal surfaces," Mech. Mater., vol. 95, pp. 102–115, 2016, doi: https://doi.org/10.1016/j.mechmat.2016.01.004.

[44] X. Sun, F. Jiang, and J. Wang, "Acoustic Properties of 316L Stainless Steel Lattice Structures Fabricated via Selective Laser Melting," Metals (Basel)., vol. 10, no. 1, 2020, doi: 10.3390/met10010111.

[45] A. Ö. Holm Altenbach, Cellular and porous materials in structures and processes / ed. by Holm Altenbach, Andreas Öchsner. Wien: Springer, 2010.

[46] S. Oller, Numerical Simulation of Mechanical Behavior of Composite Materials. 2014.

[47] R. Gümrük, R. A. W. Mines, and S. Karadeniz, "Static mechanical behaviours of stainless steel micro-lattice structures under different loading conditions," Mater. Sci. Eng. A, vol. 586, pp. 392–406, 2013, doi: https://doi.org/10.1016/j.msea.2013.07.070.

[48] *https* : *//www.ge.com/additive/*

[49] T. Zhong, K. He, H. Li, and L. Yang, "Mechanical properties of lightweight 316L stainless steel lattice structures fabricated by selective laser melting," Mater. Des., vol. 181, p. 108076, 2019, doi: https://doi.org/10.1016/j.matdes.2019.108076.

[50] B. Lozanovski et al., "Image-Based Geometrical Characterization of Nodes in Additively Manufactured Lattice Structures," 3D Print. Addit. Manuf., vol. 8, no. 1, pp. 51–68, 2021, doi: 10.1089/3dp.2020.0091.

[51] R. Saremian, M. Badrossamay, E. Foroozmehr, M. Kadkhodaei, and F. Forooghi, "Experimental and numerical investigation on lattice structures fabricated by selective laser melting process under quasi-static and dynamic loadings," Int. J. Adv. Manuf. Technol., vol. 112, no. 9, pp. 2815–2836, 2021, doi: 10.1007/s00170-020-06112-0.